HIGHLIGHTS FROM SOHO AND FUTURE SPACE MISSIONS

BERNHARD FLECK
ESA Space Science Department, NASA/GSFC Mailcode 682.3
Greenbelt, MD 20771, USA (bfleck@solar.stanford.edu)

Abstract. The Solar and Heliospheric Observatory (SOHO) has provided an unparalleled breadth and depth of information about the Sun, from its interior, through the hot and dynamic atmosphere, out to the solar wind. Analysis of the helioseismology data from SOHO has shed new light on a number of structural and dynamic phenomena in the solar interior, such as the absence of differential rotation in the radiative zone, subsurface zonal and meridional flows, sub-convection-zone mixing, a possible circumpolar jet, and very slow polar rotation. Evidence for an upward transfer of magnetic energy from the Sun's surface toward the corona has been established. The ultraviolet instruments have revealed an extremely dynamic solar atmosphere where plasma flows play an important role. Electrons in coronal holes were found to be relatively 'cool', whereas heavy ions are extremely hot and have highly anisotropic velocity distributions. The source regions for the high speed solar wind has been identified and the acceleration profiles of both the slow and fast solar wind have been measured. This paper tries to summarize some of the most recent findings from the SOHO mission. Present plans for future solar space missions are also briefly discussed.

Key words: Sun, Solar Interior, Solar Corona, Solar Wind, SOHO

1. Introduction

SOHO, the Solar and Heliospheric Observatory, is a project of international cooperation between ESA and NASA to study the Sun, from its deep core to the outer corona, and the solar wind (Domingo *et al.*, 1995). It carries a complement of twelve sophisticated instruments, developed and furnished by twelve international PI consortia involving 39 institutes from fifteen countries (Belgium, Denmark, Finland, France, Germany, Ireland, Italy, Japan, Netherlands, Norway, Russia, Spain, Switzerland, United Kingdom, and the United States). Detailed descriptions of all the twelve instruments on board SOHO as well as a description of the SOHO ground system, science operations and data products together with a mission overview can be found in Fleck *et al.* (1995).

SOHO was launched by an Atlas II-AS from Cape Canaveral Air Station on 2 December 1995, and was inserted into its halo orbit around the L1 Lagrangian point on 14 February 1996, 6 weeks ahead of schedule. Commissioning of the spacecraft and the scientific payload was completed by the end of March 1996. The launch was so accurate and the orbital maneuvers were so efficient that enough fuel remains on board to maintain the halo orbit for several decades, many times the lifetime originally foreseen (up to six years).

SOHO has a unique mode of operations, with a "live" display of data on the scientists' workstations at the SOHO Experimenters' Operations Facility (EOF) at NASA/Goddard Space Flight Center, where the scientists can command their instruments in real-time, directly from their workstations. From the very beginning SOHO was conceived as an integrated package of complimentary instruments. It was once described pointedly as an "object-oriented mission, rather than an instrument oriented mission". Great emphasis is therefore being placed on *coordinated observations*. Internally, this is facilitated through a nested scheme of planning meetings (monthly, weekly, daily), and externally through close coordination and data exchange for special campaigns and collaborations with other space missions and ground-based observatories over the Internet[1].

With over 500 articles in the refereed literature and over 1500 articles in conference proceedings and other publications, it is impossible to cover adequately all the exciting work that has been recently done. Instead, we can only touch upon some selected results.

The organization of this paper is as follows:

1 Introduction
2 Global Structure and Dynamics of the Solar Interior
    2.1 P-mode Line Profile Asymmetry
    2.2 Interior Rotation and Flows
    2.3 Interior Sound Speed Profile
3 Local Area Helioseismology
    3.1 Helioseismic Holography
    3.2 Ring Diagram Analysis
    3.3 Time-Distance Helioseismology
4 Transition Region Dynamics

[1] `http://sohowww.estec.esa.nl/operations/`

2. Global Structure and Dynamics of the Solar Interior

Just as seismology reveals the Earth's interior by studying earthquake waves, solar physicists probe inside the Sun using a technique called "helioseismology". The oscillations detectable at the visible surface are due to sound waves reverberating through the Sun's interior. These oscillations are usually described in terms of normal modes that are identified by three integers: angular degree l, angular order m, and radial order n. The frequencies of the normal modes depend on the structure and flows in the regions where the modes propagate. Because different modes sample different regions inside the Sun, by observing many modes one can, in principle, map the solar interior. By measuring precisely the mode frequencies, one can infer the temperature, density, equation of state, elemental and isotopic abundances, interior mixing, interior rotation and flows, even the age of the solar system, and pursue such esoteric matters as testing the constancy of the gravitational constant ($(1/G)\mathrm{d}G/\mathrm{d}t$), which from a recent study by Guenther *et al.* (1998) must be smaller than $1.6 \times 10^{-12}\,\mathrm{yr}^{-1}$.

2.1. P-MODE LINE PROFILE ASYMMETRY

The medium-l program of the Michelson Doppler Imager (MDI) instrument (Scherrer *et al.*, 1995) on board SOHO provides continuous observations of

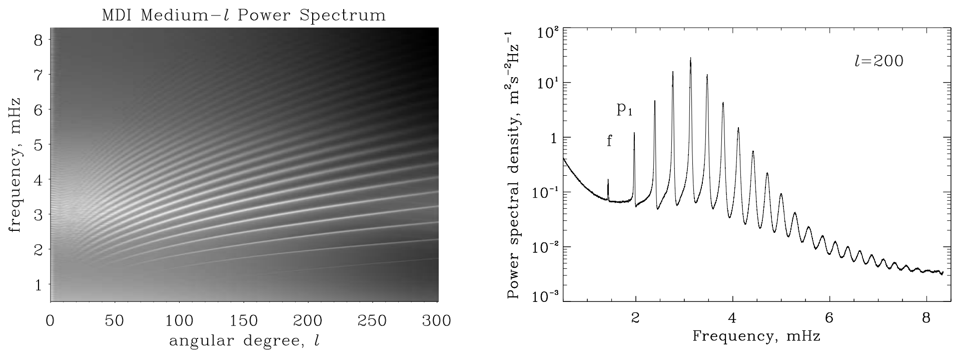

Figure 1. Left: Power spectrum ($l - \nu$ diagram) obtained from 60 days of the MDI medium-l data for m-averaged modes up to m=300 (from Kosovichev *et al.*, 1997). Right: Power spectrum obtained from 10 days of MDI medium-l data of modes l=200. Note the distinct asymmetry of the mode profiles (from Kosovichev *et al.*, 1997).

oscillation modes up to angular degree $l \approx 300$. The medium-l data are spatial averages of the full-disk Doppler velocity measured each minute. The noise in the medium-l MDI data is substantially lower than in ground-based measurements, enabling the MDI team to detect lower amplitude modes and, thus, to extend the range of measured mode frequencies. The outstanding quality of the MDI data is evident in Figure 1. Note the distinct asymmetry of the mode profiles (right diagram). In corresponding power spectra of intensity oscillations, the asymmetry is reversed. This effect is now well established and has been studied in great detail by a number of authors (e.g. Nigam *et al.*, 1998; Roxburgh and Vorontsov, 1995; Kumar and Basu, 1999). It is caused by noise – turbulent eddies at the top of the convection zone giving rise to observable intensity fluctuations – that is correlated with the oscillations.

Basu and Antia (1999) studied the effect of asymmetry in p-mode profiles on large-scale flows in the solar interior derived from ring diagram analysis. They find that the use of asymmetrical profiles leads to significant improvements in the fits, but the estimated velocity fields are not substantially different from those obtained using a symmetrical profile to fit the peaks. Rabello-Soares *et al.* (1999) showed that there is no evidence to suggest that ignoring line asymmetries in the past has compromised the helioseismic structural inversions published to date.

The degree of asymmetry depends on the relative locations of the acoustic sources and the upper reflection layer of the modes. This opens the prospect of using line profile measurements of solar modes to test theories of excitation of solar and stellar oscillations and of their interaction with turbulent convection. Kumar and Basu (1999) calculated p-mode power spectra using a realistic solar model and compared them to observed p-mode spectra from MDI and GONG. The variable parameter of their fits is the source depth of the p-modes. The depth required to fit the observed low-frequency p-mode spectra depends mainly on the nature of the sources: quadrupole sources have to be very deep between 700 and 1050 km, while dipole sources need to be relatively shallow between 120 and 350 km. From the low frequency data they used it was not possible to say whether the sources that excite solar oscillations are dipole in nature or quadrupolar. The deeper source depths of their results compared to previous studies (e.g. Nigam *et al.*, 1998) probably is due to improved solar models near the surface.

2.2. INTERIOR ROTATION AND FLOWS

The nearly uninterrupted MDI data yield oscillation power spectra with an unprecedented signal-to-noise ratio that allow the determination of the frequency splittings of the global resonant acoustic modes of the Sun with exceptional accuracy. The inversions of these data have confirmed that the decrease of the angular velocity Ω with latitude seen at the surface extends with little radial variation through much of the convection zone, at the base of which is an adjustment layer, called the "tachocline", leading to nearly uniform rotation deeper in the radiative interior (e.g. Kosovichev *et al.*, 1997, Schou *et al.*, 1998), see Figure 2. Further a prominent rotational shearing layer in which Ω increases just below the surface is discernible at low to mid latitudes. Schou *et al.* (1998) have also been able to study the solar rotation closer to the poles than has been achieved in previous investigations. The data have revealed that the angular velocity is distinctly lower at high latitudes than the values previously extrapolated from measurements at lower latitudes based on surface Doppler observations and helioseismology. This finding was confirmed and extended by Birch and Kosovichev (1998) using MDI and GONG data. Furthermore, in their landmark paper on "Helioseismic Studies of Differential Rotation in the Solar Envelope by the Solar Oscillations Investigation Using the Michelson Doppler Imager" Schou *et al.* (1998) found evidence of a submerged polar jet near latitudes of 75° which is rotating more rapidly than its immediate surroundings. The reality of this feature is still in some dispute. It is not evident in inversions of GONG data (Howe, 1998).

From f-mode frequency splittings of MDI data, Kosovichev and Schou (1997) detected zonal variations of the Sun's differential rotation, superposed on the relatively smooth latitudinal variation in Ω. These alternating zonal bands of slightly faster and slower rotation show velocity variations of about 5 m/s at a depth of 2–9 Mm beneath the surface and extend

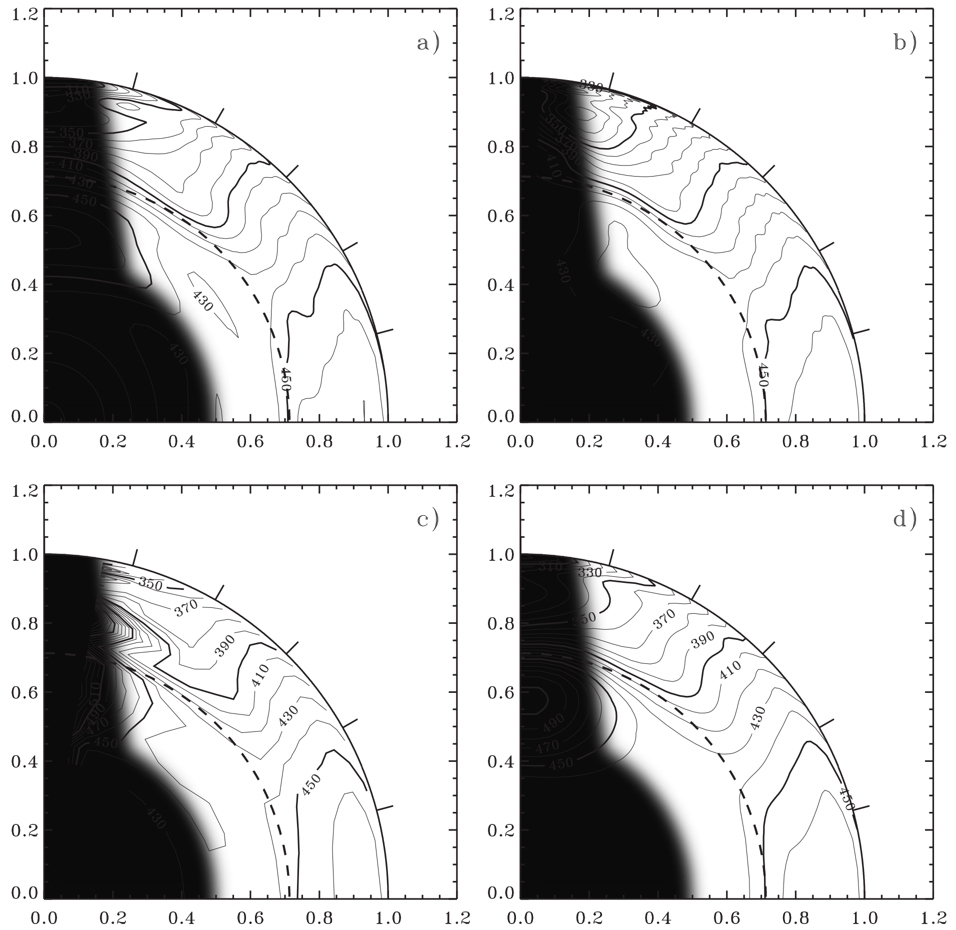

Figure 2. Solar interior rotation rate $\Omega/2\pi$ with radius and latitude for four different inversion methods: (a) 2dRLS, (b) 2dSOLA, (c) 1d1dSOLA, (d) 1.5dRLS. Some contours are labeled in nHz, and, for clarity, selected contours are shown as bold. The dashed circle indicates the base of convection zone, and the tick marks at the edge of the outer circle are at latitudes 15, 30, 45, 60, 75. In such a quadrant display, the equator is the horizontal axis and the pole the vertical one, with the proportional radius labeled. The shaded area indicates the region in the Sun where no reliable inference can be made with the current data. (From Schou *et al.*, 1998.)

some 10 to 15° in latitude. They appear to coincide with the evolving pattern of "torsional oscillations" reported from earlier surface Doppler studies (Howard and Labonte, 1980). In a later study (Schou *et al.*, 1998) these relatively weak banded flows have been followed by inversion to a depth of about 5% of the solar radius. To study the time evolution of these flows, Schou (1999) analyzed twelve 72-day time series from MDI. The inversion of the f-mode frequency splittings show a clear migration of the zonal flows

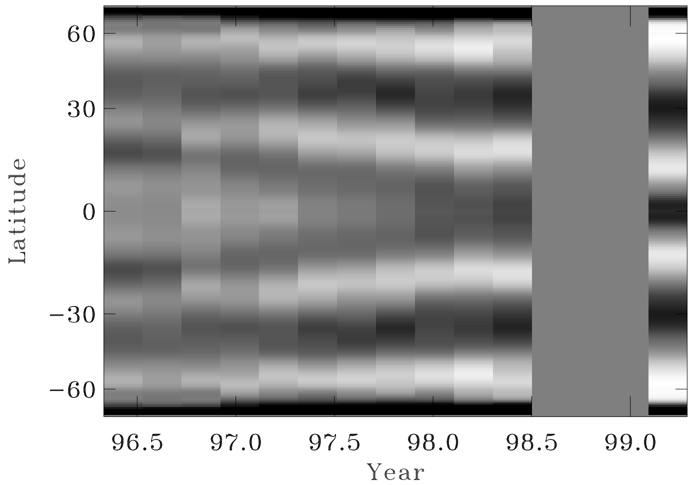

Figure 3. The zonal flows shown as a function of time and latitude. White corresponds to a prograde velocity of 7 m/s, while black corresponds to −7 m/s. The vertical axis is evenly spaced in sin (latitude). (From Schou, 1999.)

(± 7 m/s) toward the equator (Figure 3) similar to what has been seen in surface Doppler measurements or in the latitudes of the appearance of sunspots. The contrast of the bands seems to be increasing with time. He also found that the rotation rate near the poles is slower than expected from an extrapolation from lower latitudes, and seems to be changing with time. Several studies of the depth dependence of the migrating zonal flows were presented at the 9th SOHO workshop, the proceedings of which will appear as a "Topical Issue" in *Solar Physics* in Spring 2000.

Beck *et al.* (1998) have detected long-lived velocity cells in autocorrelation functions calculated from a 505 day time series of MDI data. These cells extend over 40–50 degrees of longitude but less than 10 degrees of latitude. The authors identify these cells with the elusive "giant cells", although their large aspect ratio (> 4) is surprising. It may be a consequence of the Sun's differential rotation, whereby features with a larger extent in latitude are broken up by rotational shear.

High precision MDI measurements of the Sun's shape and brightness obtained during two special 360° roll maneuvers of the SOHO spacecraft have produced the most precise determination of solar oblateness ever (Kuhn *et al.*, 1998). There is no excess oblateness. These measurements unambiguously rule out the possibility of a rapidly rotating core, and any significant solar cycle variation in the oblateness.

Armstrong and Kuhn (1999) used these MDI roll data to measure multipole shape terms of higher order than the oblateness, and compared these with helioseismic evidence for a complex internal solar rotation profile. The measured quadrupole and hexadecapole limb shapes are mildly inconsistent with current solar rotation models. The discrepancies do not appear to be resolved by the known mismatch between the helioseismic surface and Doppler surface rotation measurements.

2.3. INTERIOR SOUND SPEED PROFILE

The availability of helioseismic data of unprecedented accuracy from the SOHO MDI, GOLF, and VIRGO instruments has enabled substantial improvements in models of the solar interior (for recent reviews, see e.g. Basu, 1998; Guzik, 1998), and has shown the importance of considering mixing effects that turn out to solve existing riddles in the isotopic composition of the Sun.

The most detailed tests of solar models is being made through the inversion of differences between observed and computed mode frequencies, to determine differences in relevant physical quantities. Of particular interest in this context is the adiabatic sound speed c, or more precisely the relative difference between the squared sound speed measured in the Sun and that in models. Numerous groups have determined the spherically symmetric structure of the Sun by inverting the mean frequencies of split mode multiplets ν_{nl} from SOHO data and compared them to their latest models (e.g. Kosovichev *et al.*, 1997; Takata and Shibahashi, 1998; Brun *et al.*, 1998, 1999; Morel *et al.*, 1998).

Figure 4 shows the relative difference between the squared sound speed in the Sun as observed by GOLF and MDI and a reference model (solid line) and two models including macroscopic mixing processes in the tachocline (dashed and dash-dotted lines). Similar diagrams (as the solid line) have been produced by various groups (e.g. Basu *et al.*, 1996, Gough *et al.*, 1996; Kosovichev *et al.*, 1997; and references above). This figure is quite remarkable: There is a very good agreement between the measured sound speed and the model throughout most of the interior. Except at the conspicuous bump at about 0.68 $R_\odot$ the difference is less than 0.2%, suggesting that our understanding of the mean radial stratification of the Sun is not too far off. It was suggested that the narrow peak at about $0.68\,R_\odot$, just beneath the convection zone, may be due to a deficit of helium in this narrow region, possibly resulting from additional mixing in this layer of strong rotational shear (e.g. Kosovichev *et al.*, 1997).

In order to resolve this discrepancy and the failure of recent updated standard models to predict the photospheric lithium abundance, Brun *et al.* (1999) introduced a new term – macroscopic mixing below the convective zone – in the standard stellar structure equations. They showed that

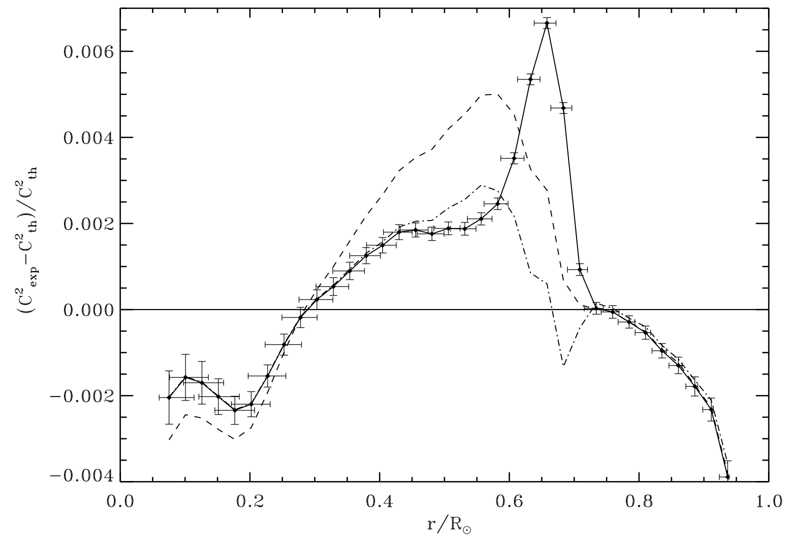

Figure 4. Relative differences between the squared sound speed in the Sun as observed by GOLF and MDI and a reference model (solid line) as well as two models including macroscopic mixing processes in the tachocline (dashed and dash-dotted lines). (From Brun *et al.*, 1999.)

the introduction of mixing in the tachocline layer partly inhibits the microscopic diffusion process and significantly improves the agreement with the helioseismic data and photospheric abundance data. In particular, the prominent bump around $0.68\,R_\odot$ in the sound-speed square difference plot is practiacally erased by the introduction of the tachocline mixing (see the dash-dotted line in Figure 4). Also, with this new term it is possible to reach the observed ^{7}Li photospheric abundance at the present solar age without destroying ^{9}Be or bringing too much ^{3}He to the surface. The solar ^{4}He primordial abundance would be slightly enriched by 10.6% to $Y_0 = 0.27$. As the process invoked concerns only the 5% part of the external mass it has little impact on the neutrino flux (only a slight reduction of a few percent).

The decrease of the sound speed compared to the model at the boundary of the energy-generating core ($\approx 0.25\,R_\odot$) in Figure 4 is not yet explained by theory. Kosovichev *et al.* (1997) speculate that the drop in sound speed may result from an overabundance of helium at the edge of the solar core.

Elliott and Gough (1999) determined the thickness of the solar tachocline by calibrating a series of solar models against sound speed measurements from MDI. The tachocline is the thin shear layer, which separates the radiative interior which rotates almost uniformly from the convection zone, where the latitudinal variation of the angular velocity Ω is observed to be more or less the same as in the photosphere. The analysis yields a value of $0.019 \pm 0.001\ R_\odot$ (formal error) for the spherically averaged full thickness Δ of the tachocline, which is somewhat smaller than previous estimates. The thickness of this layer is of great importance in assessing the magnitudes of the dominant physical processes that control the tachocline dynamics (cf. Gough and McIntyre, 1998).

3. Local Area Helioseismology

In conventional helioseismology, most results are obtained from a global mode analysis. A time series of velocity or intensity images is decomposed into eigenmodes, characterized by radial order n, spherical harmonic degree l, and azimuthal order m. The eigenfrequencies of the eigenmodes provide the global information on the spherically symmetric and axisymmetric components of the solar interior. Recently, with the availability of high spatial resolution data from MDI, interest in studying the local structure of the Sun in helioseismology has grown rapidly. There are several new techniques being developed. We mention three of them: helioseismic holography (and acoustic imaging), ring diagrams, and time-distance helioseismology. For a more comprehensive review of this new field of solar research, which is primarily developing with MDI data, see Duvall (1998).

3.1. HELIOSEISMIC HOLOGRAPHY

A technique called "helioseismic holography", originally proposed by Roddier in 1975 (although not using the term "holography"), has been applied to MDI data to render acoustic images of the absorption and egression of sunspots and active regions (Braun *et al.*, 1998; Lindsey and Braun, 1998a, 1998b). The images revealed a remarkable acoustic anomaly surrounding sunspots, now called the "acoustic moat" (Lindsey and Braun, 1998a), which is a conspicuous halo of enhanced acoustic absorption at 3 mHz. At 5–6 mHz, on the other hand, a prominent halo of enhanced acoustic emission (now called "acoustic glory") was found surrounding active regions (Braun and Lindsey, 1999). Lindsey and Braun (1999) obtained "chromatic" images over the 3–8 mHz acoustic spectrum, showing the acoustic moat out to 4.5 mHz and its disappearance at higher frequencies. Helioseismic holography essentially applies the helioseismic observations in an extended annulus surrounding the proposed source to an acoustic model of the solar interior in time reverse, regressing the acoustic field into the model interior to render images of supposed acoustic sources that can be sampled at any desired depth.

Chang *et al.* (1999) applied a similar technique called "acoustic imaging" to MDI and TON data in their search for a signature of emerging flux underneath the solar surface. They claim that, although the emerging flux below the solar surface is not easily recognized in phase-shift maps, average phase shifts over the active region reveal the signature of upward-moving magnetic flux in the solar interior. If confirmed, this could open up the possibility of studying the birth of active regions in the solar interior.

3.2. RING DIAGRAM ANALYSIS

The second technique is known as "ring diagram analysis" (Hill, 1988), which is based on the study of three-dimensional power spectra of solar p-modes on a part of the solar surface. If one considers a section of a three dimensional spectrum at fixed temporal frequency, one finds that power is concentrated along a series of rings each of which corresponds to a particular value of the radial degree n. A horizontal velocity field (U_h) present in the region in which the modes propagate produces an advection effect of the wave front and a shift in the frequencies of the modes, $\Delta\omega = k_h \cdot U_h$. Such a displacement manifests itself as an effective displacement of the centers of the rings in the constant frequency cuts. The measured frequency shifts can be inverted to obtain the horizontal flow velocities as a function of depth. Schou and Borgart (1998), Basu *et al.* (1999), and Gonzales Hernandez *et al.* (1999) applied this technique to MDI data to determine near-surface flows in the Sun. A remarkable meridional flow from the equator to the poles was found in the outermost layers of the convection zone (r $> 0.97\,R_\odot$), reaching a maximum amplitude of 25–30 m/s at approximately 30° latitude. There is some dispute about whether the amplitude of the meridional flow levels off and becomes smaller at this latitude. The flows appear to diverge close to the equator (but not exactly on the equator). No change of sign of the meridional flow has been measured, i.e. no evidence of a return flow has been detected in this depth range. The rotation rate determined with the ring diagram technique agrees well with that determined from global modes, and the measurements could be extended closer to the surface, providing new insight into the shear layer immediately beneath the surface.

3.3. TIME-DISTANCE HELIOSEISMOLOGY

The third, and perhaps most exciting and most promising technique for probing the 3-D structure and flows beneath the solar surface is called "time distance helioseismology" or "solar tomography" (Duvall *et al.*, 1993). Basically, this new technique measures the travel time of acoustic waves between various points on the surface. In a first approximation, the waves can be considered to follow ray paths that depend only on a mean solar model, with the curvature of the ray paths being caused by the increasing sound speed with depth below the surface. The travel time is affected by

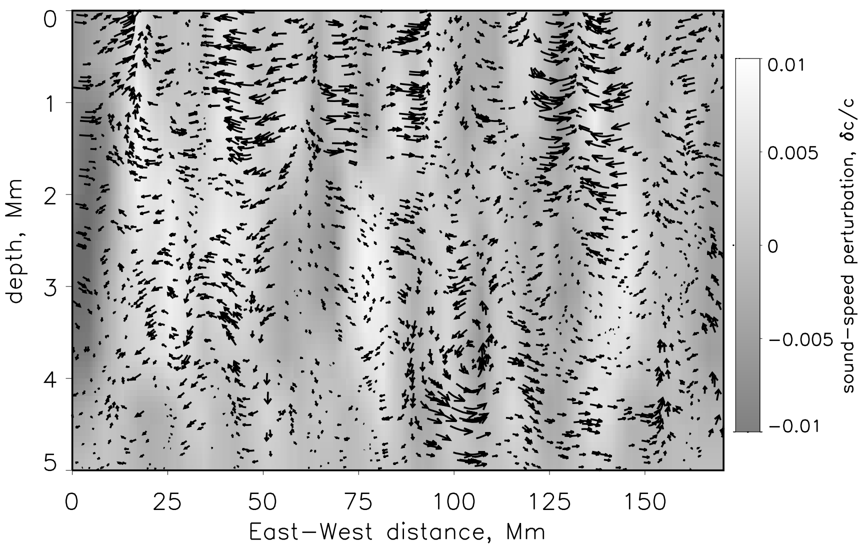

Figure 5. A vertical cut through the upper convection zone showing subsurface flows and sound speed inhomogeneities. The flow field is shown as vectors (longest arrow $1.5\,\mathrm{km\,s^{-1}}$) overlying the sound speed perturbations $\delta c/c$ (from Kosovichev and Duvall, 1997).

various inhomogeneities along the ray path, including flow, temperature inhomogeneities, and magnetic fields. By measuring a large number of times between different locations and using an inversion method, it is possible to construct 3-dimensional maps of the subsurface inhomogeneities.

By applying this new technique to high resolution MDI data, Duvall *et al.* (1997) and Kosovichev and Duvall (1997) were able to generate the first maps of horizontal and vertical flow velocities as well as sound speed variations in the convection zone just below the visible surface (Figure 5). They found that in the upper layers, 2–3 Mm deep, the horizontal flow is organized in supergranular cells, with outflows from the cell centers. The characteristic size of these cells is 20–30 Mm and the cell boundaries were found to coincide with the areas of enhanced magnetic field. The supergranulation outflow pattern disappears at a depth of approximately 5 Mm. In another attempt to determine the depth of supergranules, Duvall (1998) took the horizontal velocity at the surface determined by the tomographic inversion and cross correlated it with horizontal velocity maps at various depths. This cross-correlation function falls off very rapidly at a depth of about 4 Mm and becomes 0 at about 5 Mm. At lower depths it becomes negative – a potential indicator of a counter cell – before it returns to positive values close to zero at about 8 Mm, suggesting that the depth of the supergranular layer is about 8 Mm, i.e. only about one third of the characteristic horizontal size of the cells (20–30 Mm).

One of the most successful applications of time-distance helioseismology has been the detection of large-scale meridional flows in the solar convection zone (Giles *et al.*, 1997). Meridional flows from the equator to the poles have been observed before on the solar surface in direct Doppler shift measurements (e.g. Duvall, 1979). The time-distance measurements by Giles *et al.* (1997) provided the first evidence that such flows persist to great depths, and therefore may play an important role in the 11-year solar cycle. In their initial paper they found the meridional flow to persist to a depth of at least 26 Mm, with a depth averaged velocity of 23.5 ± 0.6 m/s at mid-latitude. In a more recent investigation Giles *et al.* (2000) extended these measurements down to a depth of $0.8\,\mathrm{R}_\odot$, without finding any evidence of a return flow. Continuity considerations led them to an estimate for the return flow below $0.8\,\mathrm{R}_\odot$ of approximately 5 m/s, which might actually be detectable in the future. Perhaps we are not too far from providing a useful constraint for dynamo theories. Giles *et al.* (2000) also measured a cross-equator flow, which in principle could be caused by a small misalignment of the MDI instrument. The depth dependence of this cross-equator flow, however, seems to be inconsistent with a possible P-angle error. Perhaps they are seeing a component of the meridional circulation which spans both hemispheres.

One of the most exciting applications of solar tomography, in particular now in the rising phase of cycle 23, is its potential for studying the birth and evolution of active regions and complexes of solar activity. Kosovichev *et al.* (2000) studied the emergence of an active region on the disk with this technique. The results show a complicated structure of the emerging region in the interior, and suggest that the emerging flux ropes travel very quickly through the upper 18 Mm of the convection zone. They estimate the speed of emergence to about 1.3 km/s, which is somewhat higher than the speed predicted by theories of emerging flux. The typical amplitude of the wave speed variations in the emerging active region is about 0.5 km/s. The observed development of the active region suggests that the sunspots are formed as a result of the concentration of magnetic flux close to the surface. Kosovichev *et al.* (2000) also present time-distance results on the subsurface structure of a large sunspot observed on 17 June 1998. The wave speed perturbations in the spot are much stronger than in the emerging flux (0.3–1 km/s). At a depth of 4 Mm, a 1 km/s wave speed perturbation corresponds to a 10% temperature variation (≈ 2800 K) or to a 18 kG magnetic field. It is interesting to note that beneath the spot the perturbation is negative in the subsurface layers and becomes positive further down in the interior. Their tomographic images also revealed sunspot "fingers" – long, narrow structures at a depth of about 4 Mm, which connect the sunspot with surrounding pores of the same polarity. Pores which have the opposite polarity are not connected to the spot.

MDI has also made the first observations of seismic waves from a solar flare (Kosovichev and Zharkova, 1998), opening up possibilities of studying both flares and the solar interior. During the impulsive phase of the X2.6 class flare of 9 July 1996 a high-energy electron beam heated the chromosphere, resulting in explosive evaporation of chromospheric plasma at supersonic velocities. The upward motion was balanced by a downward recoil in the lower chromosphere which excited propagating waves in the solar interior. On the surface the outgoing circular flare waves resembled ripples from a pebble thrown into a pond. The seismic wave propagated to at least 120,000 km from the flare epicenter with an average speed of about 50 km/s on the solar surface.

4. Transition Region Dynamics

4.1. EXPLOSIVE EVENTS AND "BLINKERS"

Several types of transient events have been detected in the quiet Sun. High-velocity events in the solar transition region, also called "explosive events", were first observed by Brueckner and Bartoe (1983), based on UV observations with HRTS. Explosive events in quiet regions have large velocity dispersions, about ± 100 km/s, i.e. velocities are directed both towards and away from the observer causing a strong line broadening.

Explosive events have been studied extensively by a number of authors using SUMER data (e.g. Innes *et al.*, 1997a, 1997b; Chae *et al.*, 1998a, 1998b; Perez *et al.*, 1999) and some results support the magnetic reconnection origin of these features. Innes *et al.* (1997b) reported explosive events that show spatially separated blue shifted and red shifted jets and some that show transverse motion of blue and red shifts, as predicted if reconnection was the source (Dere *et al.*, 1991). Comparison with MDI magnetograms and magnetograms obtained at Big Bear Solar Observatory also provided evidence that transition region explosive events are a manifestation of magnetic reconnection occurring in the quiet Sun (Chae *et al.*, 1998a). The explosive events were found to rarely occur in the interior of strong magnetic flux concentrations. They are preferentially found in regions with weak and mixed polarity, and the majority of these events occur during "cancellation" of photospheric magnetic flux (Chae *et al.*, 1998a).

Harrison *et al.* (1999) presented a thorough and comprehensive study of EUV flashes, also known as "blinkers" (Harrison, 1997), which were identified in quiet Sun network as intensity enhancements of order 10–40% using CDS. They have analyzed 97 blinker events and identified blinker spectral, temporal and spatial characteristics, their distribution, frequency and general properties, across a broad range of temperatures, from 20,000 K to 1,200,000 K. The blinkers are most pronounced in the transition region

TABLE 1. Properties of "blinkers" and explosive events.

	Blinkers	Explosive Events
Intensity:	strong brightening	little brightening
Life time:	6–40 min	1–2 min
Birth rate:	1.2 s^{-1}	600 s^{-1}
Doppler shifts:	small ($\leq$ 20 km/s)	large (100–150 km/s)
Size:	6000 $\times$ 6000 km	1500 $\times$ 1500 km
Locations:	network	edges of network brightenings

lines O III, O IV and O V, with modest or no detectable signature at higher and lower temperatures. A typical blinker has a duration of about 1000 s. Due to a long tail of longer duration events, the average duration is 2400 s, though. Comparison to plasma cooling times led to the conclusion that there must be continuous energy input throughout the blinker event. The projected blinker onset rate for the entire solar surface is 1.24 s^{-1}, i.e. at any one time there are about 3000 blinker events in progress. Remarkably, line ratios from O III, O IV and O V show no significant change throughout the blinker event, suggesting that the intensity increase is not a temperature effect but predominantly caused by increases in density or filling factor. The authors estimate the thermal energy content of an average blinker at 2×10^{25} erg.

It appears that these blinkers are also seen by EIT as He II band brightenings (Berghmans *et al.*, 1998), although they are looking at a lower temperature and report much higher global birth rate of their events (20–40 s^{-1}). The coronal events measured in Fe XII and soft X-rays in the network (e.g. Krucker *et al.*, 1997; Benz and Krucker, 1998) on the other hand seem to be a different class of events. Otherwise one would expect to have detected a signature in the Mg IX and Mg X lines in CDS data. Of particular importance is the relationship of the blinkers to the explosive events mentioned above. The typical properties of blinkers and explosive events have been summarizes in Table 1. Rather than being brightenings, the explosive events appear as extremely broad line profiles with Doppler shifts of $\pm$150 km/s. Spectral line fits to CDS data, on the other hand, have so far revealed no clear velocity shifts or only modest velocities up to a maximum of 20 km/s. Typically, the explosive events are short lived (approx. 60 sec), small scale (about $2''$) and occur at a rate of 600 s^{-1} over the Suns surface. While both types of events appear to be fairly common, it seems that they are two different classes of events. Clearly, further analysis is needed to establish the relationship between these two phenomena.

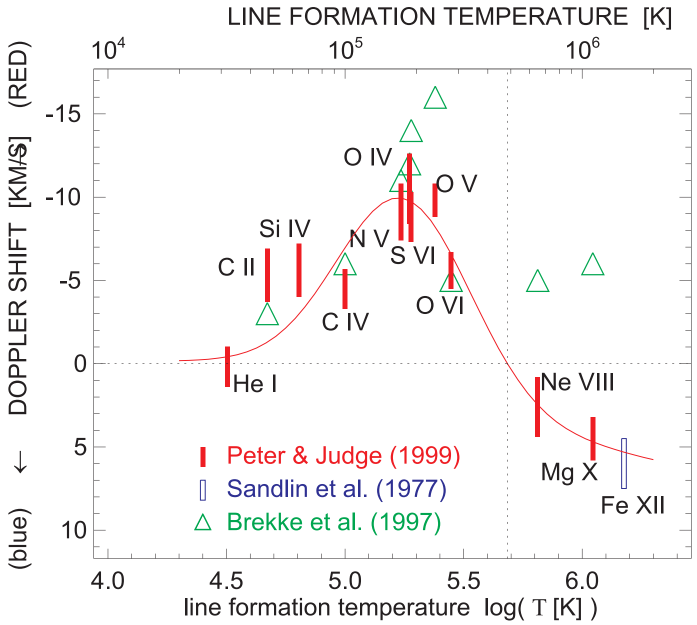

Figure 6. Variation of the Doppler shift at disk center with formation temperature of the line. Error bars for the data of Brekke *et al.* (1997a) were typically 2 km/s (not shown). The solid line is a by-eye fit to the Doppler shifts. (From Peter and Judge, 1999.)

4.2. DOPPLER SHIFTED EMISSION IN THE TRANSITION REGION

For more than two decades it has been known that the UV emission lines originating from the transition region of the quiet Sun are systematically redshifted relative to the lower chromosphere. In earlier investigations the magnitude of the redshift has been found to increase with temperature, reaching a maximum at T $\approx 10^5$ K, and then to decrease sharply toward higher temperatures (e.g. Brekke, 1993, and references therein). Systematic redshifts have also been observed in stellar spectra of late type stars, first with the International Ultraviolet Explorer (e.g., Ayres *et al.*, 1983, 1988; Engvold *et al.*, 1988) and recently by the Hubble Space Telescope (Wood *et al.*, 1996, 1997). Below temperatures of about 1.6×10^5 K, the line redshifts of the Sun, α Cen A, α Cen B, and Procyon are all very similar.

Early observations from SOHO extended the observable temperature range and suggested that the average redshift persists to higher temperatures than in most previous investigations (e.g. Brekke *et al.*, 1997a; Chae *et al.*, 1998c). Shifts in the range +10–16 km/s were observed in lines formed at T=1.3–2.5 $\times 10^5$ K (Figure 6). Even upper transition region and coronal lines (O VI, Ne VIII, and Mg X) showed systematic redshifts in the quiet Sun corresponding to velocities around +5 km/s. These measurements were made using the standard reference rest wavelengths reported in the literature (e.g. Kelly, 1987).

More recent investigations using observations with SUMER have revisited this problem. There also possible errors in rest wavelengths of lines from highly ionized atoms (e.g. Ne VIII, Na IX, Mg X, Fe XII) are discussed. Peter (1999) examined the center-to-limb variation of the Doppler shifts of C IV (1550 Å) and Ne VIII (770 Å) using full disk scans obtained with SUMER. Assuming that all effects of mass or wave motion on the limb cancel out in a statistical sense they adopt the line position on the limb as a rest wavelength. The line shifts obtained with this technique at disk center correspond to a redshift of 6 km/s for C IV and a blueshift of 2.5 km/s for Ne VIII. Similar results have been presented by Dammasch *et al.* (1999), Teriaca *et al.* (1999), and Peter and Judge (1999) who also found the Mg X line to be blueshifted by 4.5 km/s on the solar disk.

These recent results suggest that the upper transition region and lower corona appear blueshifted in the quiet Sun, with a steep transition from red- to blue-shifts above 5×10^5 K. This transition from net redshifts to blueshifts is significant because it has major implications for the transition region and solar wind modeling as well as for our understanding of the structure of the solar atmosphere. The results also motivates new laboratory measurements of the wavelengths of hotter lines since the choice of rest wavelengths used to derive these results are crucial for the interpretation of the data.

4.3. THE NETWORK

Early models of the solar atmosphere assumed that the temperature structure of the upper atmosphere was continuous with a thin transition region connecting the chromosphere with the corona. It is now apparent that this depiction is too simplistic. Rather, it appears that the solar atmosphere consists of a hierarchy of isothermal loop structures. Of particular interest in this context is the network, which is believed to be the backbone of the entire solar atmosphere and the basic channel of the energy responsible for heating the corona and accelerating the solar wind.

Patsourakos *et al.* (1999) used CDS data to study the width variation of the network with temperature. They found that the network boundaries have an almost constant width up to about 250,000 K (where the network contrast is also strongest) and then fan out rapidly at coronal temperatures. The network size in the lower transition region is about 10 arcsec and spreads to about 16 arcsec at 1 MK. These results are in very good agreement with the transition region-corona model of Gabriel (1976). The results of Feldman *et al.* (1999), on the other hand, are inconsistent with that model. They studied the morphology of the quiet solar atmosphere from 40,000 to 1,400,000 K and found no association with the chromospheric network above 900,000 K. The hottest loop structures seem to form a canopy over lower temperature loop structures and the cross-sectional areas of long coronal loops are constant to within the instrumental spatial resolution. Feldman *et al.* (1999) see difficulties reconciling these findings with the transition region-corona model of Gabriel (1976), which assumes a large scale uniform corona threaded by vertical magnetic fields. In this model, the transition region is produced by conduction back-heating from the corona. Their new observations, on the other hand, require emitting loops to be heated internally.

4.4. ACTIVE REGION DYNAMICS

EIT, SUMER, and CDS observations have clearly demonstrated that the solar transition region and corona is extremely dynamic and time variable in nature. This has become even more evident now with the advent of the spectacular high resolution time lapse sequences obtained by the Transition Region and Coronal Explorer (TRACE) (Handy *et al.*, 1999; Schrijver *et al.*, 1999). Large line shifts of up to 60 km/s were observed with CDS in individual active region loops (Brekke *et al.*, 1997b). A comprehensive investigation of active region flows by Kjeldseth-Moe and Brekke (1998) demonstrated that high Doppler shifts are common in active region loops. Strong shifts are present in parts of loops for temperatures up to 0.5 MK. Regions with both red and blue shifts are seen. While typical values correspond to velocities of ±50–100 km/s, shifts approaching 200 km/s have been detected. At temperatures $T \geq 1$ MK, i.e. in Mg IX 368 Å or Fe XVI 360 Å, only small shifts are seen. Thus, the high Doppler shifts seem to be restricted to the chromosphere and transition region.

Brynildsen *et al.* (1999) studied 3-min transition region oscillations above sunspots by analyzing time series recorded in O V 629 Å, N V 1238 Å and 1242 Å, and the chromospheric Si II 1260 Å line in NOAA 8378. The 3-min oscillations they observed above the sunspot umbra show (a) larger peak line intensity amplitudes than reported before, (b) clear signs of nonlinearities, (c) significant oscillations in line width, and (d) maxima in peak line intensity and maxima in velocity directed toward the observer that are nearly in phase (Figure 7). They also performed a simple test and calculated the velocity oscillations from the intensity oscillations (which, to a first approximation for optically thin lines, is proportional to ρ^2) using a standard text book equation for simple nonlinear acoustic waves. The agreement to the observed velocity is astounding (Figure 7, right diagram), providing convincing evidence that the oscillations they observed are upward-propagating, nonlinear acoustic waves.

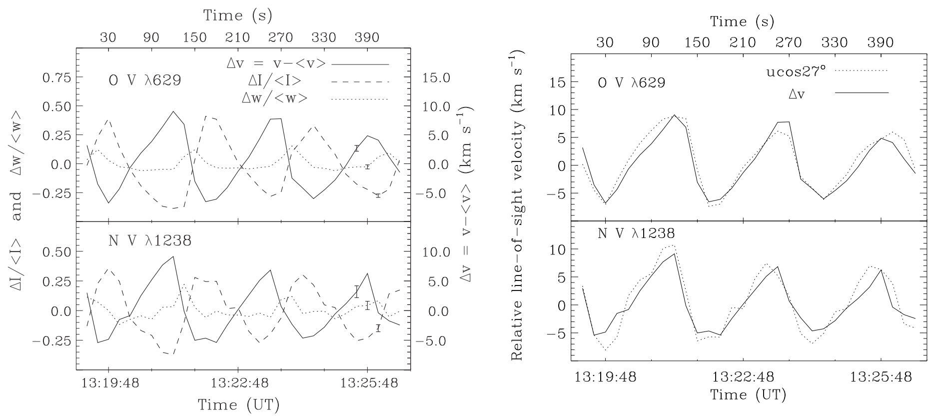

Figure 7. Left: Observed oscillations in relative line-of-sight velocity $\Delta\nu = \nu - \langle v \rangle$ (solid line), relative peak intensity $\Delta I/\langle I \rangle$ (dashed line), and relative line width $\Delta w/\langle w \rangle$ (dotted line), in the center of a sunspot umbra. Right: Temporal variations of the observed (solid line) and calculated (from the intensity variations) line-of-sight velocity $\Delta\nu$ of O V and N V. (From Brynildsen *et al.*, 1999.)

5. Corona

5.1. CORONAL HOLE TEMPERATURE AND DENSITY MEASUREMENTS

Using the two SOHO spectrometers CDS and SUMER, David *et al.* (1998) have measured the electron temperature as a function of height above the limb in a polar coronal hole (Figure 8). Temperatures of around 0.8 MK were found close to the limb, rising to a maximum of less than 1 MK at $1.15\,R_\odot$, then falling to around 0.4 MK at $1.3\,R_\odot$. In equatorial streamers, on the other hand, the temperature was found to rise constantly with increasing distance, from about 1 MK close to the limb to over 3 MK at $1.3\,R_\odot$. With these low temperatures, the classical Parker mechanims cannot alone explain the high wind velocities, which must therefore be due to the direct transfer of momentum from MHD waves to the ambient plasma.

Marsch *et al.* (1999) analyzed SUMER measurements of the Lyman series (H I Ly6, Ly7, and Ly9) obtained near the limb from about 10 to 70 arcsec and compared them to multilevel NLTE radiative transfer calculations, allowing them to derive consistently the temperatures and densitites of the hydrogen atoms at the base of the corona. The Lyman lines are broad and show the typical self-absorption reversal near the limb, where the emission comes from optically thick material, and change systematically with increasing height. The Ly6, 7, and 9 line profiles become Gaussian at about 19 to 22 arcsec above the limb. The measured temperature values range between 1×10^5 and 2×10^5 K, the densities from the model calculations were found in the range 1–2 $\times 10^8$ cm^{-3}. The turbulent contribution, ξ,

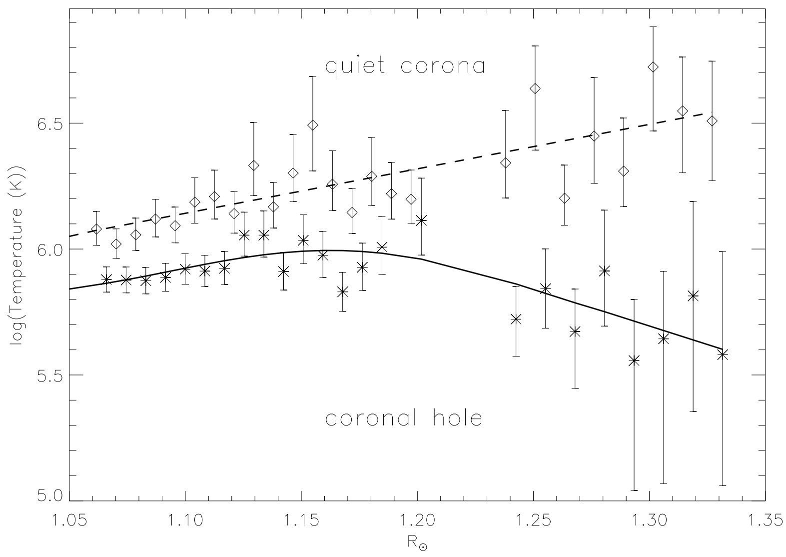

Figure 8. Temperature gradient measurement in the quiet corona (equatorial west limb) and the north polar coronal hole. (From David *et al.*, 1998.)

to the line broadenings was found to range between 20 km/s and 40 km/s, i.e. amplitues that are consistent with other estimates (Seely *et al.*, 1997; Tu *et al.*, 1998; Wilhelm *et al.*, 1998; Teriaca *et al.*, 1999) obtained in the lower coronal holes from heavy ion EUV lines formed around 10^5 K and sufficient, according to models of e.g. Tu and Marsch (1997) and Marsch and Tu (1997) to accelerate the wind to high terminal speeds between 600 and 800 km/s.

One of the most surprising results from SOHO has been the extremely broad coronal profiles of highliy ionized elements such as oxygen and magnesium (Kohl *et al.*, 1997, 1999), see Figure 9. Kohl *et al.* (1998) and Cranmer *et al.* (1999a) presented a self-consistent empirical model of a polar coronal hole near solar minimum, based on H I and O VI UVCS spectroscopic observations. Their model describes the radial and latitudinal distribution of the density of electrons, H I and O VI as well as the outflow velocity and unresolved anisotropic most probable velocities for H I and O VI (Figure 10). It provides strong evidence of anisotropic velocity distributions for protons and O VI in polar coronal holes and indicates proton outflow speeds of 190 ± 50 km/s and larger outflow speeds of 350 ± 100 km/s for O VI at 2.5 $R_\odot$ (cf. Section 6.1). While the protons (which are closely coupled to H I atoms by charge transfer in the inner corona) are only mildly anisotropic above 2–3 $R_\odot$ and never exceed 3 MK, the O VI ions are strongly anisotropic at

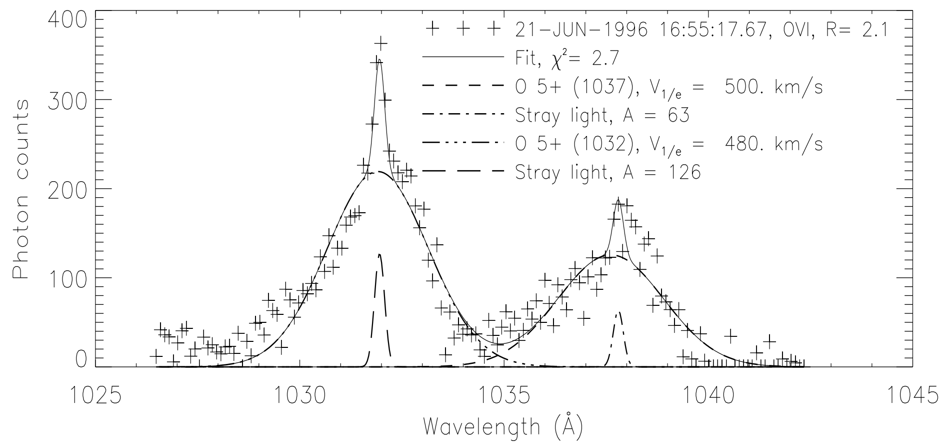

Figure 9. UVCS observations of O VI 1032 Å and 1037 Å above the north polar coronal hole at $2.1\,R_\odot$. The narrow peaks are due to straylight. The data points are shown as crosses, fitted profile by a solid line. (From Kohl *et al.*, 1997.)

these heights, with perpendicular kinetic temperatures approaching 200 MK at $3\,R_\odot$ and $(T_\perp/T_\|) \approx 10$–100 (Kohl *et al.*, 1997, 1998). The measured O VI and Mg X "temperatures" are neither mass proportional nor mass-to-charge proportional when compared to H I (Esser *et al.*, 1999; Zangrilli *et al.*, 1999). This and the highly anisotropic velocity distributions rule out thermal (common temperature) Doppler motions and bulk transverse wave motions along the line of sight as dominant line-broadening mechanisms. Clearly, additional energy deposition is required which preferentially broadens the perpendicular velocity of the heavier ions (cf. Sect. 5.3).

The electron density measured by UVCS is consistent with previous solar minimum determinations of the white-light coronal structure (Cranmer *et al.*, 1999a).

Tu *et al.* (1998) have determined ion temperatures for Ne VII, Ne VIII, Mg VIII, Mg X, Si VII, Si VIII, and heavy ions, such as Fe X, Fe XI, Fe XII in polar coronal holes above the limb (cf. also Seely *et al.*, 1997). Closer to the limb (17 to 64 arcsec) the authors find roughly constant ion temperatures for the different species, while the ion thermal speed decreases with increasing mass per charge (A/Z). At greater heights (167 to 183 arcsec above the limb), the temperature of the ions seems to increase slightly with increasing mass per charge, while the thermal speed reveals no clear trend. These measurements clearly demonstrate that the ion kinetic or effective temperatures are not equal to but significantly higher than the associated formation temperatures, and also much higher than the electron temperature reported by David *et al.* (1998) and Wilhelm *et al.* (1998).

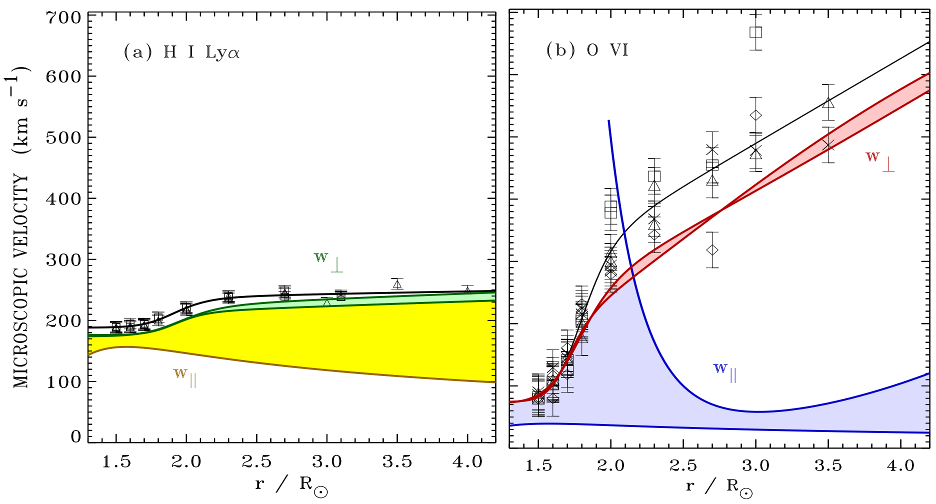

Figure 10. $v_{1/e}$ and most probable speeds for H I Lyα (left) and O VI 1032 Å (right). Squares: north polar holes, triangles: south polar holes. Solid line: best fit to data. Dotted line: most probable speed w_e corresponding to the electron temperature. (From Kohl *et al.*, 1998.)

5.2. POLAR PLUMES

Wilhelm *et al.* (1998) determined the electron temperatures, densities and ion velocities in plumes and interplume regions of polar coronal holes from SUMER spectroscopic observations of the Mg IX 706/750 Å and Si VIII 1440/1445 Å line pairs. They find the electron temperature T_e to be less than 800,000 K in a plume in the range from $r = 1.03$ to $1.60\,R_\odot$, decreasing with height to about 330,000 K. In the interplume lanes, the electron temperature is also low, but stays between 750,000 and 880,000 K in the same height interval. Doppler widths of O VI lines are narrower in the plumes ($v_{1/e} \approx 43$ km/s) than in the interplumes ($v_{1/e} \approx 55$ km/s), confirming earlier SUMER measurements by Hassler *et al.* (1997). Thermal and turbulent ion speeds of Si VIII reach values up to 80 km/s, corresponding to a kinetic ion temperature of 10^7 K.

These results clearly confirm that the ions in a coronal hole are extremely hot and the electrons much cooler. They also clearly demonstrate that local thermal equilibrium does not exist in polar coronal holes and that the assumption of Collisional Ionization Equilibrium (CIE) and the common notion that $T_e \approx T_{ion}$ can no longer be made in models of coronal holes.

It seems difficult to reconcile these low electron temperatures measured in coronal holes with the freezing-in temperatures deduced from ionic charge composition data (e.g. Geiss *et al.*, 1995). The freezing-in concept, however, assumes that the adjacent charge states are in ionization equilibrium. A critical reevaluation of this concept appears to be justified.

Previously, plumes were considered to be the source regions of the high speed solar wind. Given the narrower line widths in plumes and the absence of any significant motions in plumes, Wilhelm *et al.* (1998) suggested that the source regions of the fast solar wind are the interplume lanes rather than the plumes, since conditions there are far more suitable for a strong acceleration than those prevailing in plumes.

DeForest and Gurman (1998) observed quasi-periodic compressive waves in solar polar plumes in EIT Fe IX/X 171 Å time sequences. The perturbations amount to 10–20% of the plumes' overall intensity and propagate outward at 75–150 km/s, taking the form of wave trains with periods of 10–15 minutes and envelopes of several cycles. The authors conclude that the perturbations are compressive waves (such as sound waves or slow-mode acoustic waves) propagating along the plumes. Assuming that the waves are sonic yields a mechanical flux of $1.5–4 \times 10^5$ ergs cm^{-2} s^{-1} in the plumes. The energy flux required to heat a coronal hole is about 10^6 ergs cm^{-2} s^{-1}.

Young *et al.* (1999) published a detailed study of the temperature and density in a polar plume based on CDS measurements. Above the limb, the temperature has a narrow distribution which peaks at $1 < T < 1.1$ MK. No indications of a changing temperature with height were detected. The density from Si IX/Si X line ratios is $3.8–9.5 \times 10^8$ cm^{-3}, and exhibits no decrease with height up to 70,000 km. The background temperature seems to increase with height, which appears to be in conflict with the measurements by David *et al.* (1998). The Mg/Ne relative abundance in two strong transition region brightenings was found to be only about 1.5 times higher than the photospheric value. Thus there is no evidence of the strong Mg/Ne enhancement reported by Widing and Feldman (1992). The Ca X 557.8 Å intensity was observed 5–8 times stronger than predicted, indicating that perhaps the Arnaud and Rothenflug (1985) ion balance calculations are in error.

5.3. HEATING PROCESSES

A promising theoretical explanation for the high temperatures of heavy ions and their strong velocity anisotropies (cf. Sect. 5.1 and Figure 10) is the efficient dissipation of high-frequency waves that are resonant with ion-cyclotron Larmor motions about the coronal magnetic field lines. This effect has been studied in detail by Cranmer *et al.* (1999b), who constructed theoretical models of the nonequilibrium plasma state of the polar solar corona using empirical ion velocity distributions derived from UVCS and

SUMER. They found that the dissipation of relatively small amplitude high-frequency Alfvén waves (10–10,000 Hz) via gyroresonance with ion cyclotron Larmor motions can explain many of the kinetic properties of the plasma, in particular the strong anisotropies, the greater than mass proportional temperatures, and the faster outflow of heavy ions in the high speed solar wind. Because different ions have different resonant frequencies, they receive different amounts of heating and acceleration as a function of radius, exactly what is required to understand the different features of the H I and O VI velocity distributions. Further, because the ion cyclotron wave dissipation is rapid, the extended heating seems to demand a constantly replenished population of waves over several solar radii. This suggests that the waves are generated gradually throughout the wind rather than propagate up from the base of the corona.

In addition to measuring velocity and intensity oscillation, MDI also measures the line-of-sight component of the photospheric magnetic field. In long, uninterrupted MDI magnetogram series a continuous flux emergence of small bipolar regions has been observed (Schrijver *et al.*, 1997, 1998). Small magnetic bipolar flux elements are continually emerging at seemingly random locations. These elements are rapidly swept by granular and mesogranular flows to supergranular cell boundaries where they cancel and replace existing flux. The rate of flux generation of this "magnetic carpet" is such that all of the flux is replaced in about 40 hours (Schrijver *et al.*, 1998), with profound implications for coronal heating on the top side and questions of local field generation on the lower side of the photosphere. Estimates of the energy supplied to the corona by "braiding" of large-scale coronal field through small-scale flux replacement indicate that it is much larger than that associated with granular braiding (Schrijver *et al.*, 1998).

Preš and Phillips (1999) studied the temporal behavior of quiet Sun coronal bright points seen in EIT (Fe XII 195 Å) and Yohkoh/SXT and compared them with MDI magnetograms. They found a very good correlation between the lifetime of the bright points and the rise and fall time of magnetic flux. Estimates of the radiative losses of the bright points are much less than conductive losses, but the sum of the two was found to be comparable with the available energy of the associated magnetic field.

5.4. CORONAL MASS EJECTIONS

LASCO has been collecting an extensive database for establishing the best statistics ever on coronal mass ejections (CMEs) and their geomagnetic effects. St.Cyr *et al.* (2000) report the properties of all the 841 CMEs observed by the LASCO C2 and C3 white-light coronagraphs from January 1996 through the SOHO mission interruption in June 1998 and compare those properties to previous observations by other instruments. The CME rate for solar minimum conditions was slightly higher than had been reported for previous solar cycles, but both the rate and the distribution of apparent locations of CMEs varied during this period as expected. The distribution of apparent speeds and the fraction of CMEs showing acceleration were also in agreement with reports of earlier studies. While the pointing stability provided by the SOHO platform in its L1 orbit and the use of CCD detectors have resulted in superior brightness sensitivity for LASCO over earlier coronagraphs, they have not detected a significant population of fainter (i.e., low mass) CMEs. The general shape of the distribution of apparent sizes for LASCO CMEs is similar to those of earlier reports, but the average (median) apparent size of 72° (50°) is significantly larger.

St.Cyr *et al.* (2000) also report on a population of CMEs with large apparent sizes, which appear to have a significant longitudinal component directed along the Sun-Earth line, either toward or away from the Earth. Using full disk EIT images they found that 40 out of 92 of these events might have been directed toward the Earth. A comparison of the timing of those events with the Kp geomagnetic storm index in the days following the CME yielded that 15 out of 21 (71%) of the $\mathrm{Kp} > 6$ storms could be accounted for as SOHO LASCO/EIT frontside halo CMEs. An additional three Kp storms may have been missed during LASCO/EIT data gaps, bringing the possible association rate to 18 out of 21 (86%).

EIT has discovered large-scale transient waves in the corona, also called "Coronal Moreton Waves" and "EIT waves", propagating outward from active regions below CMEs (Thompson *et al.*, 1999). These events are usually recorded in the Fe XII 195 Å bandpass, during high-cadence (≤ 20 min) observations. Their appearance is stunning in that they usually affect most of the visible solar disk. They generally propagate at speeds of 200–500 km/s, traversing a solar diameter in less than an hour. Active regions distort the waves locally, bending them toward the lower Alfvén speed regions. Uchida (1968) and Uchida *et al.* (1973) examined a model of fast-mode Alfvén shock propagation in order to explain the chromospheric Moreton waves observed in Hα (Moreton, 1961). Their model predicted that these waves have strong coronal counterparts and that the fast-mode shock, generated by a strong impulse, would propagate through the ambient corona, where the local Alfvén speed acts as an effective index of refraction, bending the wave away from regions of strong Alfvén speed and reflecting in regions of sharp gradients. On the basis of speed and propagation characteristics, Thompson *et al.* (1999) associate the EIT waves with the fast-mode shock Moreton wave phenomenon. Another interesting aspect of these coronal Moreton waves is their association with the acceleration and injection of high energy electrons and protons (Torsti *et al.*, 1999; Krucker *et al.*, 1999).

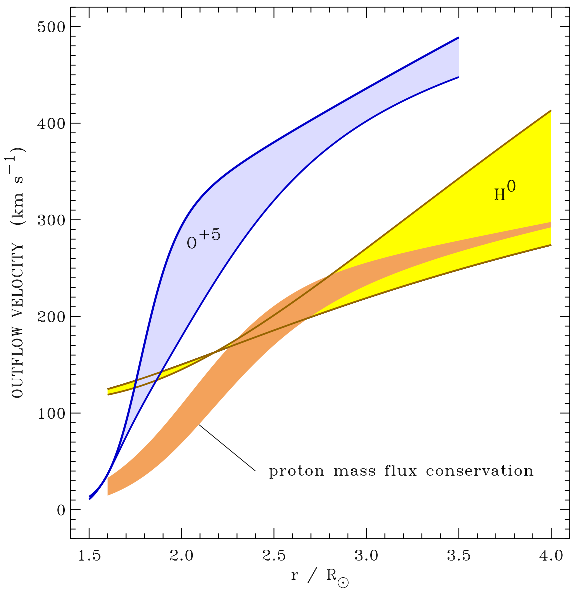

Figure 11. Empirical outflow velocity of O VI and H I in coronal holes over the poles, with gray regions corresponding to lower/upper limits of $w_{\|}$. (From Kohl *et al.*, 1998.)

6. Solar Wind

6.1. ORIGIN AND SPEED PROFILE OF THE FAST WIND

Coronal hole outflow velocity maps obtained with the SUMER instrument in the Ne VIII emission line at 770 Å show a clear relationship between coronal hole outflow velocity and the chromospheric network structure, with the largest outflow velocities occuring along network boundaries and at the intersection of network boundaries (Hassler *et al.*, 1999). This can be considered the first direct spectroscopic determination of the source regions of the fast solar wind in coronal holes.

Proton and O VI outflow velocities in coronal holes have been measured by UVCS using the Doppler dimming method (Kohl *et al.*, 1997, 1998; Li *et al.*, 1997; Cranmer *et al.*, 1999a). The O VI outflow velocity was found to be significantly higher than the proton velocity, with a very steep increase between 1.5 and 2.5 $R_\odot$, reaching outflow velocities of 300 km/s at around 2 $R_\odot$ (Figure 11). While the hydrogen outflow velocities are still consistent with some conventional theoretical models for polar wind acceleration, the higher oxygen flow speeds cannot be explained by these models. A possible explanation is offered by the dissipation of high-frequency Alfvén waves via gyroresonance with ion cyclotron Larmor motions, which can heat and accelerate ions differently depending on their charge and mass (Cranmer *et al.*, 1999b, and references therein).

6.2. SPEED PROFILE OF THE SLOW SOLAR WIND

Time-lapse sequences of LASCO white-light coronagraph images give the impression of a continuous outflow of material in the streamer belt. Density enhancements, or "blobs" form near the cusps of helmet streamers and appear to be carried outward by the ambient solar wind. Sheeley *et al.* (1997), using data from the LASCO C2 and C3 coronagraphs, have traced a large number of such "blobs" from 2 to over 25 solar radii. Assuming that these "blobs" are carried away by the solar wind like leaves on the river, they have measured the acceleration profile of the slow solar wind, which typically doubles from 150 km/s near $5\,R_\odot$ to 300 km/s near $25\,R_\odot$. They found a constant acceleration of about $4\,\mathrm{m\,s^{-2}}$ through most of the $30\,R_\odot$ field-of-view. The speed profile is consistent with an isothermal solar wind expansion at a temperature of about 1.1 MK and a sonic point near $5\,R_\odot$.

Tappin *et al.* (1999) used a similar approach as Sheeley *et al.* (1997) to determine the outflow speed of the slow solar wind. However, instead of following individual "blobs", they used cross correlation techniques. In the cross correlation functions they derived from LASCO C2 and C3 observations, they found a tail reaching out well above typical solar wind speeds, which led them to suggest that there is a high-speed component flowing out at speeds of approximately 1500 km/s, which might be energetically important and possibly dominant.

6.3. SOLAR WIND COMPOSITION

Kallenbach *et al.* (1997), using CELIAS/MTOF data, has made the first in-situ determination of the solar wind calcium isotopic composition, which is important for studies of stellar modelling and solar system formation, because the present-day solar Ca isotopic abundances are unchanged from their original isotopic composition in the solar nebula. The isotopic ratios $^{40}\mathrm{Ca}/^{42}\mathrm{Ca}$ and $^{40}\mathrm{Ca}/^{44}\mathrm{Ca}$ measured in the solar wind are consistent with terrestrial values.

The first in-situ determination of the isotopic composition of nitrogen in the solar wind has been made by Kallenbach *et al.* (1998), also based on CELIAS/MTOF data. They found an isotope ratio $^{14}\mathrm{N}/^{15}\mathrm{N} = 200 \pm 60$, indicating a depletion of $^{15}\mathrm{N}$ in the terrestrial atmosphere compared to solar matter.

Aellig *et al.* (1998) have measured iron freeze-in temperature with CELIAS/CTOF with a time resolution of 5 min. Their measurements indicate that some of the filamentary structures of the inner corona observed in Hα survive in the interplanetary medium as far as 1 AU.

Aellig *et al.* (1999) derived from CELIAS/CTOF data a value for the elemental Fe/O ratio in the solar wind. Since Fe is a low FIP element and O a high FIP element their relative abundance is diagnostic for the FIP fractionation process. The unprecedented time resolution of the CELIAS data allowed a fine scaled study of the Fe/O ratio as a function of the solar wind bulk speed. The Fe/O abundance shows a continuos decrease with increasing solar wind speed by a factor of two between 350 km/s and 500 km/s, in correspondence to the well-known FIP effect.

Using solar wind particle data from CELIAS/MTOF, Wurz *et al.* (1998) determined the abundance of the elements O, Ne, Mg, Si, S, Ca, and Fe of the January 6, 1997, CME. During the passage of the CME and the associated erupted filament, they measured an elemental composition which differs significantly from the interstream and coronal hole regions before and after this event. During the event they found a mass-dependent element fractionation with a monotonic increase toward heavier elements. The observed Si/O and Fe/O abundance ratios were about 0.4 during the CME and 0.5 during the filament passage, which is significantly higher than for typical solar wind streams.

7. Comets

SOHO is providing new measurements not only about the Sun. As of the end of November 1999 the LASCO coronagraph system has detected 87 sungrazing comets of the Kreutz family and five others (Biesecker, 1999, priv. comm.). One particular feature of these observations is the presence of a dust tail for only a few sungrazers while no tail is evident for the majority of them. Analysis of the light curves is used to investigate the properties of the nuclei (size, fragmentation, destruction) and the dust production rates (Biesecker *et al.*, 2000).

Thanks to rapid communication from the LASCO group and the near-realtime observing capabilities of the SOHO instruments due to the unique operations concept of SOHO, UVCS could make spectroscopy measurements of several comets on the day of their discovery. UVCS spectroscopic measurements of comet C/1996Y1 obtained at 6.8 $R_\odot$ confirmed the predictions of models of the cometary bow shock driven by mass-loading as cometary molecules are ionized and swept up in the solar wind. From the width and shift of the line profiles the solar wind speed at 6.8 $R_\odot$ could be determined (640 km/s). The outgassing rate of the comet was estimated at 20 kg/s, implying an active area of the nucleus of only about 6.7 m in diameter and a mass of about 120,000 kg (Raymond *et al.*, 1998).

8. Heliosphere

The Sun is moving through the Local Interstellar Cloud (LIC) at a velocity of about 26 km/s. The solar wind builds a cavity, the heliosphere, within the ionized gas component of the LIC (e.g. von Steiger *et al.*, 1996). The neutral atoms (e.g. He) of the LIC, on the other hand, enter the heliosphere unaffected. The He flow properties are now well constrained from a series of measurements ($v_{He} = 25.5 \pm 0.5$ km/s, $T_{He} = 6000 \pm 1000$ K; e.g. Möbius, 1996). These values are in agreement with measurements of the velocity and temperature of the LIC deduced from stellar spectroscopy (HST, e.g. Linksy *et al.*, 1995). Hydrogen, on the other hand, is expected to be affected by coupling with the decelerated plasma via charge-exchange. Neutral hydrogen heating and deceleration therefore provides a measurement of this coupling and in turn of the plasma density in the LIC which is responsible for most of the confinement of the heliosphere.

Costa *et al.* (1999) analysed SWAN H-cell data and compared them with a simple hot model of the interstellar H flow in the inner heliosphere. They found hydrogen temperatures T_0 of $11,500 \pm 1500$ K, i.e. significantly above the temperature of the interstellar He flow (6000 ± 1000 K), requiring a strong heating of more than 3500 K at the heliosphere interface. Part of this excess temperature probably is due to radiative transfer effects. They also measured a deceleration of the interstellar hydrogen at the heliopause of 3.5 ± 1.0 km/s.

Of particular interest for future studies might be the temperature minimum Costa *et al.* (1999) measured between the upwind and downwind direction. Classical models predict a monotonic increase of the line-of-sight temperature from upwind to downwind. The authors interpret this behaviour as first evidence of the existence of two distinct populations at different velocities, as predicted by some heliosphere-interstellar gas interface models. If confirmed, this should provide a good diagnostic of the interface.

Quémerais *et al.* (1999), in an independent study using data from the SWAN hydrogen absorption cell, determined the apparent interstellar hydrogen velocity in the up- and downwind direction to -25.4 ± 1 km/s and $+21.6 \pm 1.3$ km/s, respectively. They also presented the most precise determination (since model independent) of the H flow direction. Their new estimate of the upwind direction is $252.3° \pm 0.73°$ and $8.7° \pm 0.90°$ in ecliptic coordinates, which is off by about 3°–4° from the He flow direction. The authors speculate that this might be a sign of an asymmetry of the heliospheric interface due to the ambient interstellar magnetic field.

Comparing the above hydrogen temperature and velocity measurements by SWAN with heliospheric models leads to an estimate of the interstellar

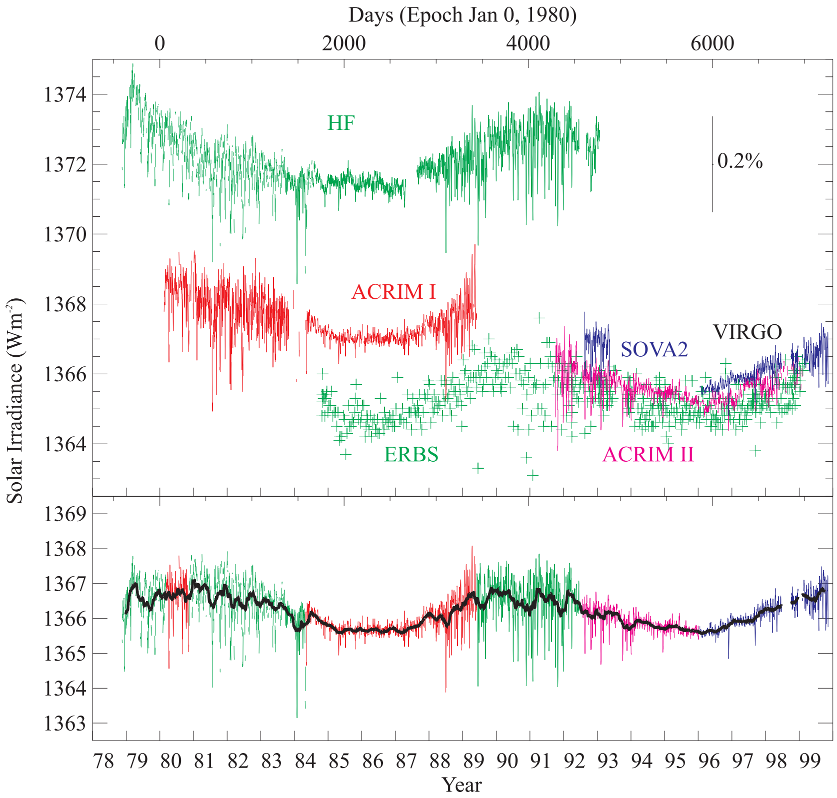

Figure 12. Total solar irradiance variations from 1978 to 1999. The data are from the Hickey-Frieden (HF) radiometer of the Earth Radiation Budget (ERB) experiment on the Nimbus-7 spacecraft (1978–1992), the two Active Cavity Radiometer Irradiance Monitors (ACRIM I and II) placed aboard the Solar Maximum Mission satellite (SMM, 1980–1989) and the Upper Atmosphere Research Satellite (UARS, 1991–), respectively, and the VIRGO radiometers flying on the SOHO (1996–). Also shown are the data from the radiometer on the Earth Radiation Budget Satellite (ERBS, 1984–), and SOVA2 as part of the Solar Variability Experiment (SOVA) on the European Retrievable Carrier (EURECA, 1992–1993). (From Quinn and Fröhlich, 1999.)

plasma density of $n_e \approx 0.04\,\mathrm{cm}^{-3}$ (Lallement, 1999). It is interesting to note that the plasma frequency for $n_e = 0.04\,\mathrm{cm}^{-3}$ is 1.8 kHz, i.e. exactly the value of the remarkably stable cut-off frequency observed by Voyager (cf. e.g. Gurnett *et al.*, 1993).

9. Total Solar Irradiance Variations

The VIRGO instrument on SOHO extends the record of total solar irradiance (TSI) measurements into cycle 23. In Figure 12 measurements from six independent space-based radiometers since 1978 (top) have been combined to produce the composite TSI over two decades (bottom). They show that the Sun's output fluctuates during each 11-year sunspot cycle, changing by about 0.1% between maxima (1980 and 1990) and minima (1987 and 1997) of solar activity. Temporary dips of up to 0.3% and a few days duration are the result of large sunspots passing over the visible hemisphere. The larger number of sunspots near the peak in the 11-year cycle is accompanied by a general rise in magnetic activity that creates an increase in the luminous output that exceeds the cooling effects of sunspots. Offsets among the various data sets are the direct result of uncertainties in the absolute radiometer scale of the radiometers ($\pm 0.3\%$). Despite these biases, each data set clearly shows varying radiation levels that track the overall 11-year solar activity cycle (cf. Fröhlich and Lean, 1998).

10. Saving SOHO

As this event determined the lives of so many of us during the summer of 1998, it seems appropriate to include a brief summary of the SOHO recovery in this paper.

At 23:16 UT on 24 June 1998, after successfully completing its nominal two-year scientific mission in April 1998, ground controllers lost contact with the SOHO spacecraft during routine maintenance operations, and the satellite went into Emergency Sun Reacquisition (ESR) mode. Efforts to re-establish nominal operations did not succeed and, after two further ESRs, telemetry was finally lost on 25 June 1998 at 04:43 UT, not to be re-established for several weeks. A SOHO Mission Interruption Joint ESA/NASA Investigation Board was established by the end of June to investigate this mishap. The Board determined that the first error was in a preprogrammed command sequence that lacked a command to enable an on-board software function designed to activate a gyro needed for control in ESR mode. The second error, which was in a different preprogrammed command sequence, resulted in incorrect readings from one of the spacecraft's three gyroscopes, which in turn triggered an ESR. The third mistake was an erroneous real-time decision which disabled part of the on-board autonomous failure detection. There was no fault on the spacecraft which contributed to the mishap.

In an attempt to recover SOHO as soon as possible, the Flight Operations Team at NASA Goddard Space Flight Center (GSFC) continued uplinking commands to the spacecraft via NASA's Deep Space Network, for at least 12 hours per day (normal pass) plus all supplementary time given by DSN. The ESA ground stations in Perth, Vilspa and Redu supported the search for a downlink signal. Special equipment was set up at the ground stations to search for spikes in the downlink spectrum and view it in real time at the SOHO operations facilities at GSFC.

Analysis by attitude experts led to the conclusion that SOHO went into a spin around an axis such that the solar panels were faced nearly edge-on towards the Sun, and thus did not generate any power. The spin axis is fixed in space and, as the spacecraft continued its orbit around the Sun, the orientation of the panels with respect to the Sun gradually changed. This resulted in a gradual increase in solar illumination of the spacecraft solar arrays.

On 23 July researchers at the National Astronomy and Ionosphere Center (NAIC) in Arecibo, Puerto Rico, using the facility's 305-meter diameter radio telescope to transmit a signal toward SOHO while the 70-meter dish of NASA's Deep Space Network in Goldstone (USA) acted as a receiver, successfully located the spacecraft using radar techniques. SOHO was found to be slowly rotating near its expected position in space.

On 3 August contact was re-established with SOHO following six weeks of silence. Short bursts of carrier signal lasting from 2 to 10 seconds were received both at the DSN station at Canberra, Australia, as well as the ESA Perth station. 37 different command procedures had been tried before this first detection of a carrier spike.

Command sequences were uplinked to divert the available solar array power into a partial charging of one of the two on-board batteries. After 10 hours of battery charging, the telemetry was commanded on and seven full sets of telemetry frames giving the spacecraft's on-board status were received on 8 August, six days after receiving the first carrier signal. Further details on the on-board conditions were obtained the following day (Sunday 9 August) in two subsequent telemetry acquisitions lasting four and five minutes respectively. Data gathered included information on the temperature of the payload instruments.

After both batteries were fully charged thawing of the hydrazine fuel in the tank was started on 12 August. It was interrupted several times during the week in order to recharge the batteries, necessary because the power data revealed a slightly negative power balance. Thawing of the hydrazine in the tank was completed on 28 August after 275 hours of tank heating. After 36 hours of recharging the batteries, heating of the first of four fuel pipe sections, which connect the tank to the thrusters, commenced on 30 August. Due to the precarious power balance it took until 10 September to thaw one of the two redundant branches of the fuel pipes. After this the batteries were recharged and the propulsion system temperature was maintained in preparation for the attitude recovery maneuver.

Finally, on 16 September, the first but important step in the SOHO recovery was successfully completed. Sun pointing (without roll control)

TABLE 2. Recovery Milestones.

Day of Year	Date	Time UT	Days from ESR 7	Events
176	25 Jun 98	04:38	–	Emergency Sun Reacquisition
176	25 Jun 98	04:43	–	Interruption of Mission
204	23 Jul 98	10:00	28	Confirmation of Orbit Position and Spacecraft Spin Rate by Arecibo and DSN Radar
215	3 Aug 98	22:51	39	Reception of Spacecraft Carrier Signal by DSN
220	8 Aug 98	23:14	44	Reception of Spacecraft Telemetry
224	12 Aug 98	23:39	48	Begin Thawing of Hydrazine Tank
240	28 Aug 98	23:02	64	End Thawing of Hydrazine Tank
242	30 Aug 98		66	Begin Thawing of Hydrazine Lines
259	16 Sep 98	05:45	83	Start of Attitude Recovery
259	16 Sep 98	18:29	83	ESR 8
259	16 Sep 98	18:30	83	SOHO lock to Sun
266	21 Sep 98	16:58	90	SOHO in RMW mode
268	25 Sep 98	17:30	92	Orbit Correction (first segment)
268	25 Sep 98	19:52	92	SOHO in Normal Mode
278	5 Oct 98	18:21	102	Start of Instrument Recommissioning
309	5 Nov 98		133	Completion of Instrument Recommissioning

was achieved at 18:30 UT, after a gradual despin of the spacecraft followed by a (planned this time ...) Emergency Sun Reacquisition. All operations went according to plan.

After a busy week of recommissioning activities of the various spacecraft subsystems and an orbit correction maneuver, SOHO was finally brought back to normal mode on 25 September at 19:52:58 UT. Miraculously, the only equipment failure at spacecraft level were two of the three gyros. All other subsystems work as well as they did before the loss of contact, and no redundancy has been lost. Table 2 lists the milestones of the SOHO recovery (see also Figure 13). For a more detailed and more technically oriented account the reader is referred to "SOHO's Recovery – An Unprecedented Success Story" by F. Vandenbussche (1999).

From thermal models which were confirmed by housekeeping data received on 9 August it was known that the instruments went through an ordeal of extreme temperatures, with some instruments being baked at almost $+100^\circ$ C, while others were subjected to a deep freeze of less than -120° C. The twelve experiment teams therefore were anxiously awaiting the moment when they could switch on and check out their instruments.

On 5 October a four week period of instrument recommissioning began. Flight software, electronics and mechanisms of all instruments were reval-

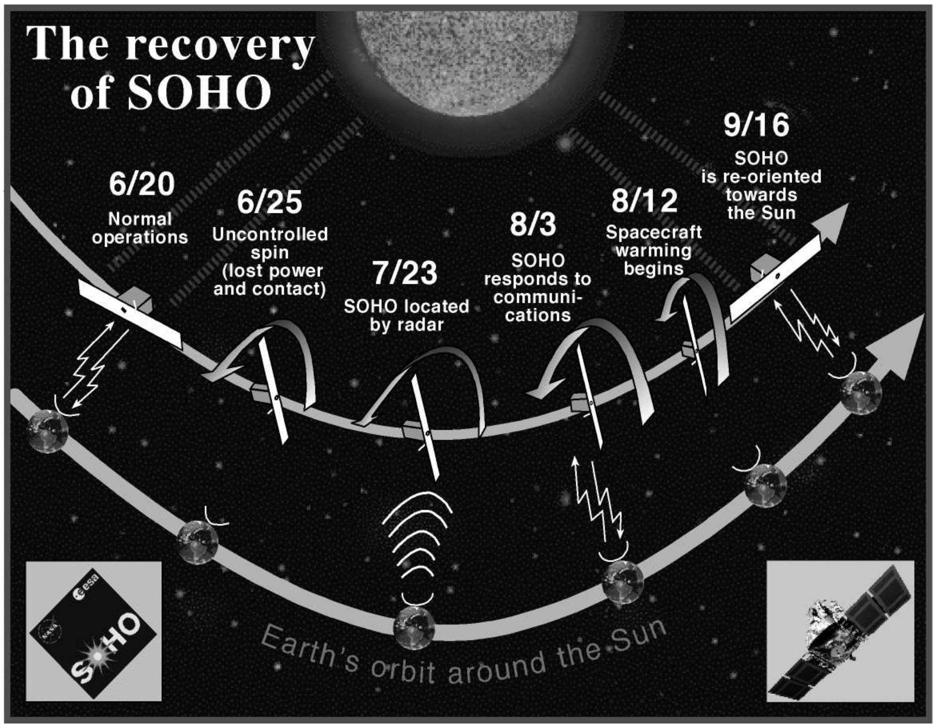

Figure 13. Milestones of the SOHO recovery.

idated, followed by a thorough recalibration of the sensors, spectrometers and cameras. The recommissioning of the instruments was completed on 5 November. Miraculously, all twelve instruments (with the exception of the LASCO C1 coronagraph) work as well as they did before the unfortunate loss-of-contact, and sometimes even better, despite the extremes in heat and cold that they have been subjected to.

The fact that both the spacecraft as well as all twelve instrument survived this ordeal with minor scars constitutes a great tribute to the skill, dedication and professionalism of the scientists and engineers who designed and built these instruments and this spacecraft. The recovery team was led by Francis Vandenbussche from ESA's Scientific Projects Department and comprised engineers from ESA, Matra Marconi Space and other European industries, NASA, and the AlliedSignal Flight Operations Team (FOT). Thanks to the extraordinary efforts of the recovery team (Figure 14), rewarded by this astounding accomplishment of successful recovery of the mission, the solar community can now be looking forward to an exciting and scientifically rewarding solar maximum.

Figure 14. Some of the members of the SOHO Recovery Team at NASA/GSFC on 17 September 1998.

11. Future Missions

11.1. MISSIONS IN DEVELOPMENT

11.1.1. *HESSI*

HESSI, the High Energy Solar Spectroscopic Imager, is scheduled for launch on July 4th, 2000 as part of NASA's Small Explorer Program. HESSI's primary mission is to explore the basic physics of particle acceleration and explosive energy release in solar flares. The HESSI mission consists of a single spin-stabilized spacecraft in a low-altitude orbit inclined 38 degrees to the Earth's equator. The only instrument on board is an imaging spectrometer with the ability to obtain high fidelity "color movies" of solar flares in X-rays and gamma rays. It uses two new complementary technologies: fine grids to modulate the solar radiation, and germanium detectors to measure the energy of each photon very precisely. HESSI's imaging capability is achieved with fine tungsten and gold grids that modulate the solar X-ray flux as the spacecraft rotates at approximately 15 rpm. Up to 20 detailed images can be obtained per second. High-resolution spectroscopy (2–5 keV) is achieved with 9 cooled germanium crystals that detect the X-ray and gamma-ray photons transmitted through the grids over the broad energy range of 3 keV to 20 MeV. More information can be found at: `http://hesperia.gsfc.nasa.gov/hessi/`.

11.2. MISSIONS UNDER STUDY

11.2.1. *Solar-B*

Solar-B is a joint Japan/US/UK/German mission (lead by ISAS) proposed as a follow-on to the highly successful Japan/US/UK Yohkoh (Solar-A) collaboration. The mission consists of a coordinated set of optical, EUV and X-ray instruments that will investigate the interaction between the Sun's magnetic field and its corona. The objective is to obtain an improved understanding of the mechanisms which give rise to solar magnetic variability and how this variability modulates the total solar output and creates the driving force behind space weather. The proposed Solar-B instrument complement comprises three packages:

- Solar Optical Telescope (SOT), comprising a 50 cm aperture optical telescope and a Focal Plane Package (FPP) consisting of a Vector Magnetograph operating in the visible and a Littrow type echelle spectrograph for detailed Stokes line profiles of intensity and polarization.
- X-Ray Telescope (XRT), operating in the wavelength range 2–60 Å with a resolution of 1 to 2.5 arcsec, and
- EUV Imaging Spectrograph (EIS), operating in the temperature range from $1 \times 10^5 - 2 \times 10^7$ K and providing Doppler line shifts and widths and monochromatic images.

Solar-B is presently under study, with a target launch date in fall 2004. More information can be found at `http://wwwssl.msfc.nasa.gov/ssl/pad/solar/solar-b.htm`.

11.2.2. *STEREO*

STEREO is a two-spacecraft mission aimed at a better understanding of the origin and consequences of CMEs and thereby improving our science base for space wheather predictions. Two identical spacecraft will image the Sun and sample the heliospheric environment at gradually increasing angular separations from Earth. Spacecraft #1 will lead the Earth by 45 degrees after 2 years, spacecraft #2 will lag the Earth by 50 degrees after 2 years. The following four instrument packages have been selected by NASA:

- Sun Earth Connection Coronal and Heliospheric Investigation (SECCHI), which consists of four instruments: an Extreme Ultraviolet Imager, two white-light coronagraphs and a Heliospheric Imager. SECCHI's integrated instruments will study the 3-D evolution of CME's from birth at the Sun's surface through the corona and interplanetary medium to its eventual impact at Earth.
- STEREO/WAVES (SWAVES), an interplanetary radio burst tracker that will track the generation and evolution of traveling radio disturbances from the Sun to the orbit of Earth.

- In situ Measurements of Particles and CME Transients (IMPACT), which will sample the 3-D distribution and provide plasma characteristics of solar energetic particles and the local vector magnetic field.
- PLAsma and SupraThermal Ion and Composition (PLASTIC), which will provide plasma characteristics of protons, alpha particles and heavy ions.

More information can be found at `http://sd-www.jhuapl.edu/STEREO/`.

11.3. PROPOSED MISSIONS

11.3.1. *NASA Sun-Earth Connection Roadmap*

NASA just issued its new Sun-Earth Connection (SEC) Roadmap – Strategic Planning for 2000–2025. The goal of the new SEC theme is "to understand our changing Sun and its effcts on the solar system, life, and society". The strategy for understanding this interactive system is organized around four fundamental Quests, designed to answer the following questions:

1 Why does the Sun vary?
2 How do the planets respond to solar variations?
3 How do the Sun and galaxy interact?
4 How does solar variability affect life and society?

The new mid-term plan (launch in 2008–2014) includes two solar missions of the Solar-Terrestrial Probes class ($\leq$ \$250M) and one solar mission of the new Frontier Probes class ($\geq$ \$250M). The two STP missions are

- SONAR (Solar Near-surface Active-region Rendering)
- RAM (Reconnection and Microscale probe)

and the new Frontier mission is

- SPI (Solar Polar Imager).

In addition there is the Solar Probe in the current "Outer Planets Program".

Other solar missions mentioned in the new NASA SEC roadmap are:

- High Resolution Solar Optical Telescope (aiming at a resolution of 50 milli-arcsec or better)
- Particle Acceleration Solar Orbiter (PASO)
- Solar Far Side Oberserver
- Solar Flotilla (multiple microsatellites in solar elliptic orbits)

11.3.2. *ESA F2/F3 Opportunities*

On 1 October 1999 ESA issued a call for two "Flexi" or "F-missions" (F2 and F3), each for a maximum cost of 176 MEURO. A total of 39 Letters of Intent (plus one for NGST, which is expected to be selected for F2) were received by 22 October 1999, three of which are solar:

- Solar Orbiter (SO) – a high resolution mission to the Sun and inner heliosphere. The most interesting and novel observations would be made in almost heliosynchronous segments of the orbits at heliocentric distances near $45\,R_\odot$ (allowing high spatial resolution with moderate size instruments) and out-of ecliptic up to 38°.
- Next Generation SOHO – a two-spacecraft ESA/NASA partnership, building on the huge success of SOHO. Core objectives of this mission include acoustic tomography of the convection zone and sub-surface active region structure as well as high spatial/high temporal resolution UV/EUV imaging and spectroscopy.
- Solar Physics and Interferometry Mission (SPI) – a new generation high resolution solar physics mission, the core of which would be an UV interferometer, consisting of three 35 cm telescopes cophased on a 1 m baseline with active pointing. Target resolution of this instrument is 0.02 arcsec.

Deadline for proposals is 31 January 2000, selection is expected for fall 2000, following an assessment phase lasting from 1 March to end May 2000.

With the treasure of SOHO data alrady in the SOHO archive (and many more data yet to come, hopefully well beyond the next solar maximum) and the splendid ideas for future missions, the future of solar physics appears to look very bright. Eventually we should be able to overcome our ignorance of how our daylight star works.

Acknowledgements

The great success of the SOHO mission is a tribute to the many people who designed and built this exquisite spacecraft and these excellent instruments, and to the many people who diligently work behind the scenes to keep it up and running. Special thanks go to Harold W. Benefield and his AlliedSignal Flight Operations Team, Helmut Schweitzer and Jean-Philippe Olive from the ESA/MMS Technical Support Team, the Science Operations Coordinators Laura Roberts, Joan Hollis and Piet Martens, the SOHO Science Data Coordinator Luis Sanchez, Craig Roberts, John Rowe and their colleagues from Flight Dynamics, the colleagues from DSN, Francis Vandenbussche and his recovery team for making a miracle come true, and, last but not least, to the original Project Scientists Vicente Domingo and Art Poland for their leadership, which was crucial in ensuring the scientific success of this mission.

References

Aellig, M.R., Grünwald, H., Bochsler, P., *et al.*: 1998, *JGR* **103**, 17 215.
Aellig, M.R., Hefti, S., Grünwald, H., *et al.*: 1999, *JGR* **104**, 24 769.
Armstrong, J. and Kuhn, J.R.: 1999, *ApJ* **525**, 533.
Arnaud, M. and Rothenflug, R.: 1985, *A&A Suppl.* **60**, 425.
Ayres, T.R., Stencel, R.E., Linsky, J.L., *et al.*: 1983, *ApJ* **274**, 801.
Ayres, T.R., Jensen, E., and Engvold, O.: 1988, *ApJ Suppl.* **66**, 51.
Basu, S.: 1998, in J. Provost and F.-X. Schmider (eds.), *Sounding Solar and Stellar Interiors*, Proc. IAU Symp. 181, Kluwer, 137.
Basu, S., Christensen-Dalsgaard, J., Schou, J., Thompson, M.J., and Tomczyk, S.: 1996, *Bull. Astr. Soc. India* **24**, 147.
Basu, S., Antia, H.M., and Tripathy, S.C.: 1999, *ApJ* **512**, 458.
Basu, S. and Antia, H.M.: 1999, *ApJ* **525**, 517.
Beck, J.G., Duvall, T.L., and Scherrer, P.H.: 1998, *Nature* **394**, 653.
Benz, A.O. and Krucker, S.: 1998, *Solar Phys.* **182**, 349.
Berghmans, D., Clette, F., and Moses, D.: 1998, *A&A* **336**, 1039.
Biesecker, D.A.: 1999, *priv. comm.*
Biesecker, D.A., *et al.*: 2000, *in prep.*
Birch, A.C. and Kosovichev, A.G.: 1998, *ApJ* **503**, L187.
Braun, D.C., Lindesy, C., Fan, Y., and Fagan, M.: 1998, *ApJ* **502**, 968.
Braun, D.C. and Lindsey, C.: 1999, *ApJ* **513**, L79.
Brekke, P.: 1993, *ApJ* **408**, 735.
Brekke, P., Hassler, D.M., and Wilhelm, K.: 1997a, *Solar Phys.* **175**, 349.
Brekke, P., Kjeldseth-Moe, O., and Harrison, R.A.: 1997b, *Solar Phys.* **175**, 511.
Brueckner, G.E. and Bartoe, J.-D.F.: 1983, *ApJ* **272**, 329.
Brun, A.S., Turck-Chieze, S., and Morel, P.: 1998, *ApJ* **506**, 913.
Brun, A.S., Turck-Chieze, S., and Zahn, J.P.: 1999, *ApJ* **525**, 1032.
Brynildsen, N., Kjeldseth-Moe, O., and Maltby, P.: 1999, *ApJ* **517**, L159.
Chae, J., Wang, H. , Lee, C.-Y., Goode, P.R., and Schühle, U.: 1998a, *ApJ* **497**, L109.
Chae, J., Wang, H. , Lee, C.-Y., Goode, P.R., and Schühle, U.: 1998b, *ApJ* **504**, L123.
Chae, J., Yun, H.S., and Poland, A.I. 1998c, *ApJ Suppl.* **114**, 151.
Chang, H.-K., Chou, D.-Y., and Sun, M.-T.: 1999, *ApJ* **526**, L53.
Costa, J., Lallement, R., Quémerais, E., Bertaux, J.-L., Kyrölä, E., and Schmidt, W.: 1999, *A&A* **349**, 660.
Cranmer, S.R., Kohl, J.L., Noci, G., *et al.*: 1999a, *ApJ* **511**, 481.
Cranmer, S.R., Field, G.B., and Kohl, J.L.: 1999b, *ApJ* **518**, 937.
Dammasch, I.E., Wilhelm, K., Curdt, W., and Hassler, D.M.: 1999, *A&A* **346**, 285.
David, C., Gabriel, A.H., Bely-Dubau, F., Fludra, A., Lemaire, P., and Wilhelm, K.: 1998, *A&A* **336**, L90.
DeForest, C.E. and Gurman, J.B.: 1998, *ApJ* **501**, L217.
Dere, K.P., Bartoe, J.-D.F., Brueckner, G.E., Ewing, J., and Lund, P.: 1991, *JGR* **96**, 9399.
Domingo,V., Fleck, B., and Poland, A.I.: 1995, *Solar Phys.* **162**, 1.
Duvall, T.L., Jr.: 1979, *Solar. Phys.* **63**, 3.
Duvall, T.L., Jr.: 1998, in S. Korzennik and A. Wilson (eds.), *Proc. SOHO-6/GONG 98 Workshop*, ESA SP-418, 581.
Duvall, T.L., Jr., Jefferies, S.M., Harvey, J.W., and Pomerantz, M.A.: 1993, *Nature* **379**, 235.
Duvall, T.L., Jr., Kosovichev, A.G., Scherrer, P.H., *et al.*: 1997, *Solar Phys.* **170**, 63.
Elliott, J.R. and Gough, D.O.: 1999, *ApJ* **516**, 475.
Engvold, O., Ayres, T.R., Elgarøy, Ø., *et al.*: 1988, *ApJ* **192**, 234.
Esser, R., Fineschi, S., Dobrzycka, D., *et al.*: 1999, *ApJ* **510**, L63.
Feldman, U., Widing, K.G., and Warren, H.P.: 1999, *ApJ* **522**, 1133.

Fleck, B., Domingo, V., and Poland, A.I. (eds.): 1995, The SOHO Mission, *Solar Phys.* **162**, Nos. 1–2.
Fröhlich, C. and Lean, J.: 1998, *GRL* **25**, 4377.
Gabriel, A.H.: 1976, *Phil. Trans. R. Soc. London* **A281**, 575.
Geiss, J., Gloeckler, G., von Steiger, R., *et al.*: 1995, *Science* **268**, 1033.
Giles, P.M., Duvall, T.L., Jr., and Scherrer, P.H.: 1997, *Nature* **390**, 52.
Giles, P.M., Duvall, T.L., Jr., and Scherrer, P.H.: 2000, *Solar Phys.*, submitted.
Gonzalez Hernandez, I., Patron, J., Bogart, R.S., and the SOI Ring Diagram Team: 1999, *ApJ* **510**, L153.
Gough, D.O., Kosovichev, A.G., and Toomre, J., *et al.*: 1996, *Science* **272**, 1296.
Gough, D.O. and McIntyre, M.E.: 1998, *Nature* **394**, 755.
Guenther, D.B., Krauss, L.M., and Demarque, P.: 1998, *ApJ* **498**, 871.
Gurnett, D.A., Kurth, W.S., Allendorf, S.C., and Poynter, R.L.: 1993, *Science* **262**, 199.
Guzik, J.A.: 1998, in S. Korzennik and A. Wilson (eds.), *Proc. SOHO-6/GONG 98 Workshop*, ESA SP-418, 417.
Handy, B.N., Acton, L.W., and Kankelborg, C.C., *et al.*: 1999, *Solar Phys.* **187**, 229.
Hassler, D.M., Wilhelm, K., Lemaire, P., and Schühle, U.: 1997, *Solar Phys.* **175**, 375.
Hassler, D.M., Dammasch, I., Lemaire, P., Brekke, P., Curdt, W., Mason, H.E., Vial, J.-C., and Wilhelm, K.: 1999, *Science* **283**, 810.
Harrison, R.A.: 1997, *Solar Phys.* **175**, 467.
Harrison, R.A., Lang, J., Brooks, D.H., and Innes, D.E.: 1999, *A&A* **351**, 1115.
Hill, F.: 1988, *ApJ* **333**, 996.
Howard, R. and LaBonte, B.J.: 1980, *ApJ* **239**, L33.
Howe, R.: 1998, in S. Korzennik and A. Wilson (eds.), *Proc. SOHO-6/GONG 98 Workshop*, ESA SP-418, 669.
Innes, D.E., Brekke, P., Germerott, D., and Wilhelm, K.: 1997a, *Solar Phys.* **175**, 341.
Innes, D.E., Inhester, B., Axford, W.I., and Wilhelm, K.: 1997b, *Nature* **386**, 811.
Kallenbach, R., Ipavich, F.M., Bochsler, P., *et al.*: 1997, *ApJ* **498**, L75.
Kallenbach, R., Geiss, J., Ipavich, F.M., *et al.*: 1998, *ApJ* **507**, L185.
Kelly, R.L.: 1987, *J. of Physical and Chemical Reference Data* **16**, Suppl. No. 1.
Kjeldseth-Moe, O. and Brekke, P.: 1998, *Solar Phys.* **182**, 73.
Kohl, J.-L., Noci, G., and Antonucci, E., *et al.*: 1997, *Solar Phys.* **175**, 613.
Kohl, J.-L., Noci, G., Antonucci, E., *et al.*: 1998, *ApJ* **501**, L127.
Kohl, J.-L., Esser, R., and Cranmer, S.R., *et al.*: 1999, *ApJ* **510**, L59.
Kosovichev, A.G. and Duvall, T.L.: 1997, in J. Christensen-Dalsgaard and F. Pijpers, *Solar Convection and Oscillations and their Relationship*, Proc. of SCORe'96 Workshop, Aarhus (Denmark), Kluwer, Acad. Publ, 241.
Kosovichev, A.G. and Schou, J.: 1997, *ApJ* **482**, L207.
Kosovichev, A.G., Schou, J., Scherrer, *et al.*: 1997, *Solar Phys.* **170**, 43.
Kosovichev, A.G. and Zharkova, V.V.: 1998, *Nature* **393**, 317.
Kosovichev, A.G., Duvall, T.L., and Scherrer, P.H.: 2000, *Solar Phys.*, submitted.
Krucker, S., Benz, A., Action, L.W., and Bastian, T.S.: 1997, *ApJ* **488**, 499.
Krucker, S., Larson, D.E., Lin, R.P., and Thompson, B.J.: 1999, *ApJ* **519**, 864.
Kuhn, J.R., Bush, R.I., Scheick, X., and Scherrer, P.H.: 1998, *Nature* **392**, 155.
Kumar, P. and Basu, S.: 1999, *ApJ* **519**, 389.
Lallement, R.: 1999, in S. Habbal *et al.* (eds.), *Proc. Solar Wind 9*, AIP Conf. Proc. 471, 205.
Li, X., Esser, R., Habbal, S.R., and Hu, Y.-Q.: 1997, *JGR* **102**, 17419.
Lindsey, C. and Braun, D.C.: 1998a, *ApJ* **499**, L99.
Lindsey, C. and Braun, D.C.: 1998b, *ApJ* **509**, L129.
Lindsey, C. and Braun, D.C.: 1999, *ApJ* **510**, 494.
Linsky, J.L., Diplas, A., Wood, B.E., *et al.*: 1995, *ApJ* **451**, 335.
Marsch, E., and Tu, C.-Y.: 1997, *A&A* **319**, L17.
Marsch, E., Tu, C.-Y., Heinzel, P., Wilhelm, K., and Curdt, W.: 1999, *A&A* **347**, 676.
Möbius, E.: 1996, *Space Sci. Rev.* **78**, 375.

Morel, P., Provost, J., and Berthomieu, G.: 1998, in S. Korzennik and A. Wilson (eds.), *Proc. SOHO-6/GONG 98 Workshop*, ESA SP-418, 499.
Moreton, G.F.: 1961, *S&T* **21**, 145.
Nigam, R., Kosovichev, A.G., Scherrer, P.H., and Schou, J.: 1998, *ApJ* **495**, L115.
Patsourakos, S., Vial, J.-C., Gabriel, A.H., and Bellamine, N.: 1999, *ApJ* **522**, 540.
Perez, M.E., Doyle, J.G., Erdelyi, R., and Sarro, L.M.: 1999, *A&A* **342**, 279.
Preś, P. and Phillips, K.J.H.: 1999, *ApJ* **510**, L73.
Peter, H.: 1999, *ApJ* **516**, 490.
Peter, H. and Judge, P.G.: 1999, *ApJ* **522**, 1148.
Quémerais, E., Bertaux, J.-L., Lallement, R., and Berthé, M.: 1999, *JGR* **104**, 12 585.
Quinn, T.J. and Fröhlich, C.: 1999, *Nature* **401**, 841.
Rabello-Soares, M.C., Christensen-Dalsgaard, J., Rosenthal, C.S., and Thompson, M.J.: 1999, *A&A* **350**, 672.
Raymond, J.C., Fineschi, S., Smith, P.L., *et al.*: 1998, *ApJ* **508**, 410.
Roddier, F.: 1975, *CR Acad. Sci. Paris* **281**, B993.
Roxburgh, I.W. and Vorontsov, S.V.: 1995, *MNRAS*, **272**, 850.
Scherrer, P.H., Bogard, R.S., and Bush, R.I., *et al.*: 1995, *Solar Phys.* **162**, 129.
Schou, J.: 1999, *ApJ* **523**, L181.
Schou, J. and Bogart, R.S.: 1998, *ApJ* **504**, L131.
Schou, J., Antia, H.M., Basu, S., *et al.*: 1998, *ApJ* **505**, 390.
Schrijver, C.J., Title, A.M., van Ballegooijen, A., Hagenaar, H.J., and Shine, R.A.: 1997, *ApJ* **487**, 424.
Schrijver, C.J., Title, A.M., Harvey, K.L., *et al.*: 1998, *Nature* **394**, 152.
Schrijver, C.J., Title, A.M., Berger, T.E., *et al.*: 1999, *Solar Phys.* **187**, 261.
Seely, J.F., Feldman, U., Schühle, U., Wilhelm, K., Curdt, W., and Lemaire, P.: 1997, *ApJ* **484**, L87.
Sheeley, N.R. Jr., Wang, Y.-M., Hawley, S.H., *et al.*: 1997, *ApJ* **484**, 472.
St.Cyr, C., Howard, R.A., Sheeley, N.R., Jr., *et al.*: 2000, *JGR*, submitted.
Takata, M. and Shibahashi, H.: 1998, *ApJ* **504**, 1035.
Tappin, S.J., Simnett, G.M., and Lyons, M.A.: 1999, *A&A*, 350, 302.
Teriaca, L., Banerjee, D., and Doyle, J.D.: 1999, *A&A* **349**, 636.
Thompson, B.J., Gurman, J.B., Neupert, W.M., *et al.*: 1999, *ApJ* **517**, L151.
Torsti, J., Kocharov, L., Teittinen, M., and Thompson, B.J.: 1999, *ApJ* **510**, 460.
Tu, C.-Y., Marsch, E.: 1997. *Solar Phys.* **109**, 149.
Tu, C.-Y., Marsch, E., Wilhelm, K., and Curdt, W.: 1998, *ApJ* **503**, 475.
Uchida, Y.: 1968, *Solar Phys.* **4**, 30.
Uchida, Y., Altschuler, M.D., and Newkirk, G. Jr.: 1973, *Solar Phys.* **39**, 431.
Vandenbussche, F.: 1999, *ESA Bull.* **97**, 39.
von Steiger, R., Lallement, R., and Lee, M. (eds): 1996, The Heliosphere in the Local Interstellar Cloud, *Space Sci. Rev.* **78**, Nos. 1–2.
Widing, K.G. and Feldman, U.: 1992, *ApJ* **392**, 715.
Wilhelm, K., Marsch, E., Dwivedi, B.N., *et al.*: 1998, *ApJ* **500**, 1023.
Wood, B.E., Harper, G.M., Linsky, J.L., and Dempsey, R.C.: 1996, *ApJ* **458**, 761.
Wood, B.E., Linsky, J.L., and Ayres T.R.: 1997, *ApJ* **487**, 745.
Wurz, P., Ipavich, F.M., Galvin, A.B., *et al.*: 1998, GRL **25**, 2557.
Young, R.R., Klimchuk, J.A., and Mason, H.E.: 1999, *A&A* **350**, 286
Zangrilli, L., Nicolosi, P., Poletto, G., Noci, G., Romoli, M., and Kohl, J.L.: 1999, *A&A* **342**, 592